
A DYNAMIC CLAMP PROTOCOL TO ARTIFICIALLY MODIFY CELL CAPACITANCE

Paul Pfeiffer^{1,2}, Federico José Barreda Tomás^{2,3}, Jiameng Wu^{2,4}, Jan-Hendrik Schleimer^{1,2}, Imre
Vida^{2,3}, Susanne Schreiber^{1,2*}

¹Institute for Theoretical Biology, Humboldt-Universität zu Berlin, Philippstr. 13, Haus 4, 10115 Berlin, Germany

²Bernstein Center for Computational Neuroscience, Humboldt-Universität zu Berlin, Philippstr. 13, Haus 6, 10115
Berlin, Germany

³Institute for Integrative Neuroanatomy, Charité-Universitätsmedizin Berlin, Corporate Member of Freie Universität
Berlin, Humboldt-Universität zu Berlin, and Berlin Institute of Health, Charitéplatz 1, 10117 Berlin, Germany

⁴Einstein Center for Neurosciences Berlin, Berlin, Germany

*For correspondence: s.schreiber@hu-berlin.de

ABSTRACT

1 **Abstract** - Dynamics of excitable cells and networks depend on the membrane time constant, set
2 by membrane resistance and capacitance. Whereas pharmacological and genetic manipulations of
3 ionic conductances are routine in electrophysiology, experimental control over capacitance remains
4 a challenge. Here, we present capacitance clamp, an approach that allows to mimic a modified
5 capacitance in biological neurons via an unconventional application of the dynamic clamp technique.
6 We first demonstrate the feasibility to quantitatively modulate capacitance in a mathematical neuron
7 model and then confirm the functionality of capacitance clamp in *in vitro* experiments in granule cells
8 of rodent dentate gyrus with up to threefold virtual capacitance changes. Clamping of capacitance
9 thus constitutes a novel technique to probe and decipher mechanisms of neuronal signaling in ways
10 that were so far inaccessible to experimental electrophysiology.

11 **1 Introduction**

12 Membrane capacitance is a major biophysical parameter in neurons and other excitable cells, which determines how
13 fast the membrane potential changes in response to a current [1, 2]. How capacitance impacts electrical signaling and
14 neuronal processing, however, can rarely be observed experimentally, because its value appears to be constant for most
15 membranes, around 1.0 uF/cm² [3]. A prominent exception is the reduced capacitance of myelinated axons, which
16 allows faster action potential propagation [4] and thereby crucially contributes to cognitive functions [5]. The effects
17 of capacitance changes can, therefore, so far only be compared via mathematical simulations, where capacitance is
18 simple to control. Such modeling, for example, suggests that the reduced membrane capacitance observed in human
19 pyramidal cells can serve to increase synaptic efficacy [6; but see 7]. Nevertheless, experimental manipulation of
20 capacitance remains challenging; in particular because changes in membrane area, thickness and lipid composition that
21 affect capacitance might influence other membrane functions, such as the embedding of ion channels, with potentially
22 unintended and uncontrolled consequences for electrical behavior. Here, we address this technical challenge by
23 introducing capacitance clamp (CapClamp): an intracellular recording mode based on the dynamic clamp that emulates
24 altered capacitance values in biological neurons [8, 9]. Via CapClamp, the voltage dynamics governed by the actual
25 biophysics of a cell – active ion channels and synaptic inputs – can thus be flexibly probed under multiple “virtual”
26 capacitance conditions, which provides precise experimental control over this hitherto inaccessible parameter.

27 In addition to the analysis of biological capacitance adaptations, control over capacitance offers a distinct way to probe
28 cellular electrical dynamics. Capacitance has a unique temporal role, because its direct effects are restricted to the
29 membrane time constant whilst leaving the steady state I-V curve unaltered. In this way, capacitance differs from leak
30 conductance, the other determinant of the time constant, which also alters steady-state response amplitudes. For this
31 reason, theoretical studies preferentially vary capacitance to investigate ion channel dynamics [10, 11] and qualitative
32 switches (bifurcations) in neural excitability [12, 13]. Furthermore, effects of an altered capacitance can be informative
33 about more complex, time scale-related parameters like temperature or ion concentrations [14]. Such computational
34 predictions, however, often rely on simplified neuron models, so a similar experimental control over capacitance would
35 be desirable to test them in biological cells.

36 The proposed CapClamp alters capacitance in a virtual manner, combining the simplicity of computational control with
37 the complex biophysics of a real neuron. It is inspired by the dynamic clamp technique, which has originally been
38 developed to simulate the presence of additional conductances in a biological neuron relying on a fast feedback loop
39 between intracellular recording and a computational model [8, 9, 15, 16]. The precise control over virtual conductances
40 enables electrophysiological experiments that are more difficult or even impossible with traditional pharmacological
41 or genetic means [17–22]. Here, we demonstrate how the dynamic clamp can be extended to virtual capacitance
42 modifications by currents designed to speed up or slow down dynamics of the membrane potential. We derive a simple
43 expression for these CapClamp currents, which can be applied in all excitable cells and only requires the experimenter
44 to specify the original cell and the desired target capacitance. In an experiment based on a hardware-implemented

45 RC circuit, we verify that the CapClamp indeed correctly modifies the time constant. Via numerical simulations, we
46 confirm that a clamped model neuron exhibits the same pronounced changes of firing and spike shape as a control cell
47 with an altered capacitance. For an experimental demonstration, we clamp the near-somatic capacitance of rat dentate
48 gyrus granule cells and analyze how the induced local capacitance change affects their spiking behavior. Finally, we
49 illustrate how the CapClamp can be used to probe signal integration, energy consumption and bifurcations of excitable
50 cells in ways that so far were experimentally inaccessible.

51 **2 Results**

52 **2.1 Capacitance clamp: a dynamic clamp protocol to mimic capacitance changes**

53 Dynamic clamp relies on a fast feedback loop between an intracellular recording of a neuron and a computer that
54 simulates virtual cellular or circuit components online. Originally, the dynamic clamp has been developed to study
55 how a membrane conductance alters the neuron’s voltage dynamics [8, 9]. In each recording interval (i.e. time interval
56 between two voltage samplings), a digital model of the conductance receives the sampled membrane potential, updates
57 the conductance state and sends the corresponding current value back to the amplifier. In this way, given a sufficiently
58 high update rate f_{dyn} (often ≥ 10 kHz), the current through the recording electrode accurately mimics the current
59 through the modeled conductance and the dynamics of the neuron appear as if this conductance was physically present
60 in the membrane.

61 Whereas conductances gate ionic currents across the membrane, the capacitance determines how fast these currents
62 can change the membrane potential. Every altered membrane property that results in a modified capacitance value,
63 such as membrane area, thickness or lipid composition, affects this rate of change of the membrane potential (Fig. 1 A).
64 To artificially mimic a modified capacitance, we therefore first asked whether a dynamic clamp protocol with its fast
65 feedback loop between voltage sampling and current injection could adjust the “speed” of a cell’s membrane potential
66 (Fig. 1 B). Using the current balance equation, the basic mathematical description of membrane voltage dynamics, we
67 derived a capacitance clamp (CapClamp) scheme with a simple expression for the clamping current I_{dyn} (see Methods),

$$I_{\text{dyn},i} = \frac{C_c - C_t}{C_t} \left(C_c \frac{V_i - V_{i-1}}{\Delta t} - I_{\text{dyn},i-1} \right), \quad (1)$$

68 which only requires the experimenter to measure the cell capacitance C_c in order to set a new target capacitance C_t .
69 In every recording interval $\Delta t = f_{\text{dyn}}^{-1}$, the CapClamp uses the measured cell capacitance value C_c and the voltage
70 derivative $\frac{V_i - V_{i-1}}{\Delta t}$ to estimate the present membrane current and then increases ($C_t < C_c$) or decreases ($C_c < C_t$)
71 the net current by insertion of a correction current in the next time bin. In this way, despite a physically unaltered
72 capacitance, the membrane potential changes faster or, respectively, slower – as if the clamped cell actually had the
73 different capacitance C_t selected by the experimenter. In the following, we will demonstrate the CapClamp in simulated

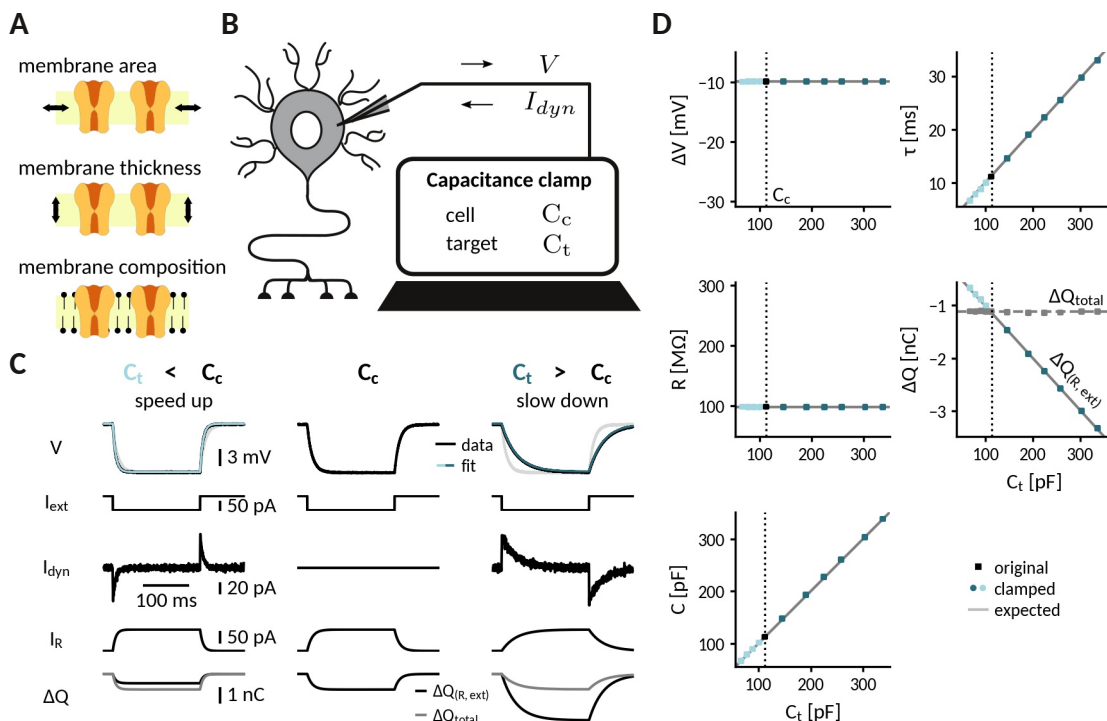


Figure 1: **Adding or removing artificial capacitance via the CapClamp.** **A** Physically, membrane capacitance varies with surface area, thickness and lipid composition **B** Virtual capacitance modification via the CapClamp is a form of dynamic clamp, a fast feedback between intracellular voltage sampling and computer-controlled current injection: given the measured cell capacitance C_c , the target capacitance C_t and recorded membrane potentials, the computer calculates clamping currents required to mimic the desired change of capacitance. **C** Clamping a hardware-implemented model cell (RC circuit) at a decreased (left) or increased (right) capacitance leads to faster respectively slower charging of the “membrane potential” V (top row, exp: black traces, exponential fit: light and dark blue) in response to a step current I_{ext} (2nd row) due to the clamping currents I_{dyn} (3rd row). As a result, the current through the resistance $I_R = -\frac{V}{R}$ (4th row) has a different profile and the apparently deposited charge $\Delta Q(R, ext) = \int dt I_R + I_{ext}$ (5th row, black) by the “cellular” transmembrane currents decreases, respectively, increases as expected for a capacitance change. The total deposited charge ΔQ_{total} (gray), taking into account the clamping currents, is the same in all three cases, because the physical capacitance did not change. **D** Measured time constant τ , voltage responses ΔV , resistance R , deposited charge ΔQ (apparent and total) and capacitance C versus target capacitances.

74 and experimental scenarios with increasing complexity ranging from a passive RC circuit up to biological neurons with
75 a spatially extended morphology.

76 2.2 Clamping capacitance in a passive cell

77 The simplest scenario to apply the CapClamp is a single compartment passive cell, equivalent to an RC circuit. In the
78 absence of active conductances, the effects of a capacitance change can be precisely formulated: the capacitance C sets
79 the membrane time constant $\tau = RC$, determining how fast the membrane potential changes in response to a current.
80 Note that, in contrast to the resistance R , the change in capacitance leaves the voltage amplitude of the steady-state
81 response unaltered. To quantitatively confirm the effects of clamping capacitance and the ability of an exclusively
82 temporal control, we measured time constant and capacitance of a clamped RC circuit in experiment and analyzed the
83 temporal filtering properties of a modeled clamped circuit using mathematical analysis.

84 To experimentally characterize a clamped passive cell, we implemented the CapClamp scheme in a dynamic clamp setup
85 (see Methods) and recorded voltage responses to current pulses from the simplest possible model cell, i.e., a hardware
86 implemented RC circuit, while clamping it at a range of target capacitances (Fig. 1 C). As expected for an RC circuit,
87 the charging curve of the unclamped model cell was fit well by a single exponential, whose time constant ($\tau=11.1$ ms)
88 and voltage amplitude ($\Delta V=-9.9$ mV) allowed us to determine the circuit's resistance $R=99.4$ M Ω and capacitance
89 $C=112.3$ pF. This capacitance value was then used as the cell capacitance C_c input for the CapClamp. Clamped
90 at a decreased capacitance, the time constant shortened ($C_t=67.4$ pF: $\tau=6.6$ ms) and at an increased capacitance,
91 it lengthened ($C_t=336.9$ pF: $\tau=33.0$ ms), but in both cases the steady state voltage amplitude remained the same.
92 Accordingly, the measured capacitance of the clamped circuit confirmed the chosen target capacitance for the whole
93 tested range from a 0.6- up to a 3-fold change with respect to the original capacitance (e.g. $C_t=67.4$ pF: $C=67.5$ pF;
94 $C_t=336.9$ pF: $C=338.1$ pF), whereas the measured resistance remained constant (Fig. 1 D).

95 As a consequence of the correctly transformed voltage response, the leak current in the clamped RC circuit also behaved
96 as if the capacitance had changed. When the circuit was clamped, the leak current through the resistance, $I_R = \frac{V}{R}$,
97 exhibited a shorter ($C_t < C_c$) or longer ($C_t > C_c$) transient until reaching steady state. As a consequence, the charge
98 $\Delta Q(I_R, I_{ext})$ deposited on the capacitance by the apparent "transmembrane" current, the sum of leak and external
99 stimulus current, reduced ($C_t < C_c$) or increased ($C_t > C_c$) to the extent expected for an altered capacitance (Fig. 1
100 C). In contrast, the overall deposited charge $\Delta Q(I_R, I_{ext}, I_{dyn})$, including the clamping current, was identical in the
101 clamped and the original circuit, reflecting that the physical capacitance did not change. For the simple RC circuit
102 considered here, the distinction between the clamping current and the intrinsic "cellular" currents might appear artificial,
103 because all currents use the same charge carrier. In a biological neuron, however, this distinction becomes relevant,
104 because the clamping currents through the recording electrode might rely on other charge carriers (depending on the
105 used intracellular solution) than the cellular currents governed by multiple ion selective channel types.

106 For more complex stimuli than a simple current pulse, the temporal filtering properties of a clamped membrane
107 determine how well the CapClamp mimics the chosen capacitance change. To generally assess these filtering properties,
108 we analytically derived the frequency-dependent impedance of a modeled clamped RC circuit using linear control
109 theory (Fig. 1 - suppl. 1 A, see Appendix). The derived impedance profiles confirmed the experimentally observed
110 altered time constants. For example, an RC circuit clamped at an increased capacitance further attenuated non-zero
111 frequencies reflecting its longer time constant. Overall, impedance amplitudes of a clamped RC and the corresponding
112 target circuit fit well up to a tenth of the dynamic clamp frequency f_{dyn} , that is up to ≈ 2 kHz for a 20 kHz dynamic
113 clamp system as used here (Fig. 1 - suppl. 1 B and C). As high frequencies are heavily attenuated by the low pass filter
114 of a cell's membrane, these differences lead to relatively small deviations in the voltage responses. The mathematical
115 analysis thus suggests that for a fast dynamic clamp system (>20 kHz), the CapClamp is expected to work well for most
116 stimuli with time scales in the physiological range.

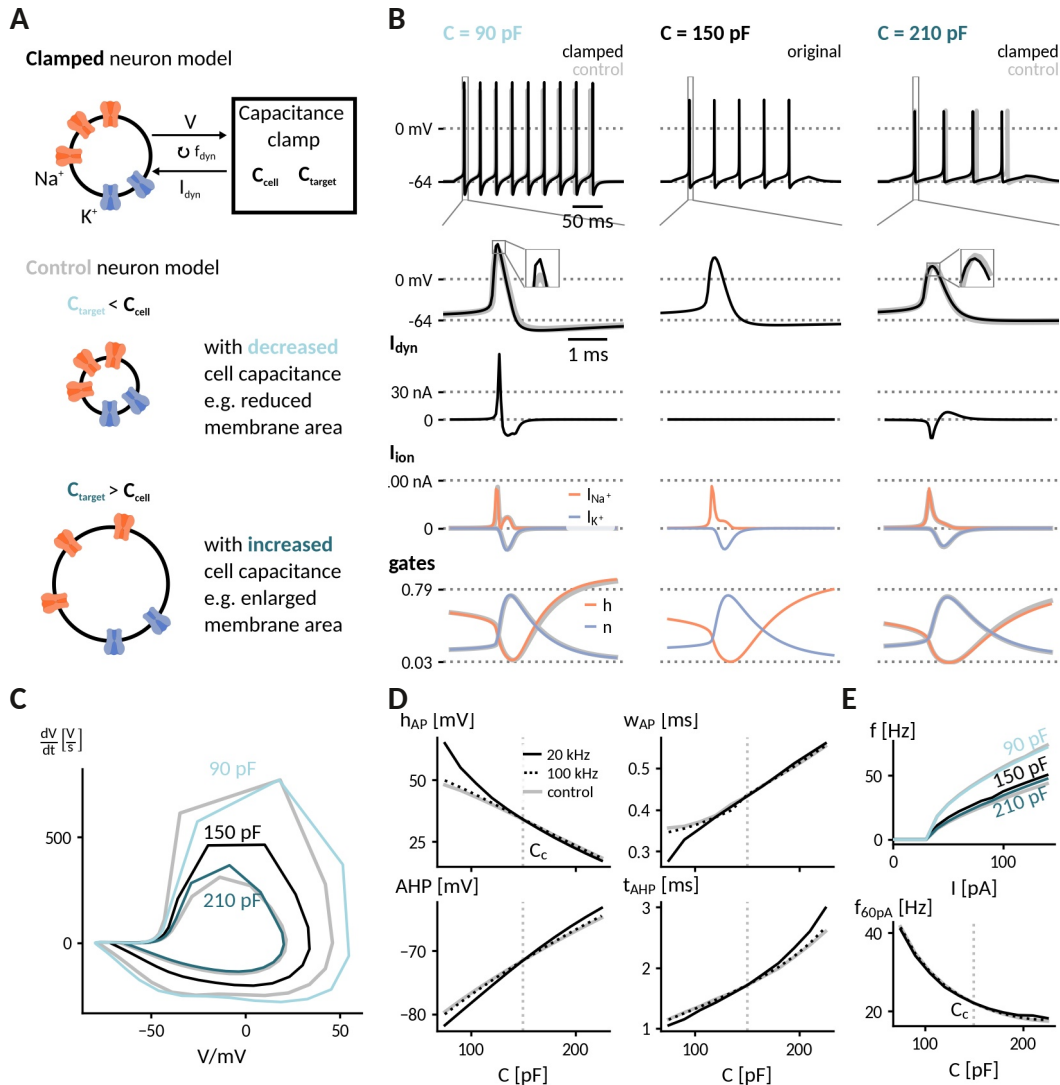


Figure 2: Simulation of the capacitance clamp in a conductance based neuron model. **A** Neurons coupled to the CapClamp are compared with control neurons with an altered capacitance (depicted as a difference in membrane area). **B** Spiking at 0.6-fold decreased (90 pF), original (150 pF) and 1.4-fold increased capacitance (210 pF) with from top to bottom: spike shape, dynamic clamp current, ionic currents (Na^+ , K^+) and gating states (h: sodium inactivation gate, n: potassium activation gate). Clamped and original traces in black or color, control in gray. **C** Comparison of spike shapes in the V - $\frac{dV}{dt}$ -plane (black: original, blues: clamped, gray: control). **D** Comparison of spike amplitude h_{AP} (top left), spike width w_{AP} (top right), after hyperpolarization amplitude AHP (lower left) and timing t_{AHP} (lower right) across different capacitances with two dynamic clamp frequencies (solid: 20 kHz, dotted: 100 kHz, gray: control). **E Top**: Comparison of f-I curves for capacitances in B. **Bottom**: Comparison of firing frequency at 60 pA across different capacitances with two dynamic clamp frequencies (solid: 20 kHz, dotted: 100 kHz, gray: control).

117 2.3 Simulation of the CapClamp in a biophysical neuron model

118 In neurons with active spike-generating conductances, capacitance changes impact neuronal firing via the interplay
119 of the altered membrane time constant and the gating kinetics of the channels involved. As gating dynamics can be
120 in the sub-millisecond range, e.g. for transient sodium channels, the CapClamp is expected to require a sufficiently
121 high dynamic clamp frequency to accurately reproduce changes of spike shape or firing rate. To understand these
122 requirements and lay the ground for investigations of capacitance changes in biological neurons, we simulated the
123 CapClamp in a neuron model with biophysical channel dynamics and a single-compartment morphology (see Methods).
124 The simulation allowed us to compare the firing of the clamped neuron to the expected firing at this modified capacitance.
125 Specifically, we inspected the spiking responses to a depolarizing current for the original 150 pF, a decreased 90 pF and
126 an increased 210 pF capacitance, for the latter two comparing clamped and expected dynamics (Fig. 2 A). Capacitance
127 changes exerted a notable influence on both firing frequency and spike shape, which was mostly well-captured by
128 the simulated CapClamp (Tab. 1). When the capacitance was decreased to 90 pF, spiking frequency speeded up and
129 action potentials had a larger peak amplitude, a decreased duration and an increased afterhyperpolarization (AHP).
130 When the capacitance was increased to 210 pF, the effects were opposite: spiking frequency slowed down and action
131 potentials had a smaller peak, an increased duration and a reduced AHP. At increased capacitances, spike amplitudes of
132 the clamped neuron were larger than expected, a consequence of the limited tracking of the fast sodium current at the
133 used dynamic clamp frequency (Fig. 2 B). Except for this brief overshoot, the CapClamp overall forced the membrane
134 potential on the expected trajectory and correctly adjusted the resulting ionic currents and the gating variable dynamics
135 of the active conductances, e.g. for a reduced capacitance of 90 pF, the sodium current became narrower in time and
136 exhibited a second peak (Fig. 2 A).

137 A subsequent comparison of simulated spiking for the whole range of tested target capacitances from 75 pF to 225 pF
138 confirmed that the CapClamp reliably reproduced the main effects of a modified capacitance on spike shape (Fig. 2 C)
139 and firing frequency (Fig. 2 D). As expected, a crucial factor for a good quantitative fit is the dynamic clamp frequency –
140 observable differences at a 20 kHz sampling frequency were strongly reduced for a sampling frequency of 100 kHz
141 (Fig. 2 C and D). In this regard, the chosen neuron model is especially demanding because its rapid gating dynamics are
142 fit to a fast spiking interneuron [23]. Taken together, our simulations show that capacitance impacts neuronal spiking
143 from firing frequency to action potential shape and that the CapClamp is well-suited to study these effects.

Table 1: Firing frequency and spike shape in a biophysical neuron model for a decreased, the original and an increased capacitance, comparing simulations of an actually altered capacitance with the CapClamp. Values are shown as actual(**clamped**).

C (pF)	f (Hz)	h_{AP} (mV)	w_{AP} (ms)	AHP (mV)
decreased 90	34.9(34.3)	45.7(55.0)	0.30(0.30)	-77.8(-79.7)
original 150	22.1	33.9	0.39	-71.5
increased 210	17.8(18.9)	21.4(20.1)	0.48(0.48)	-66.0(-64.7)

144 **2.4 Experimental demonstration of the CapClamp in rat dentate gyrus granule cells**

145 Biological neurons differ from the simple “cells” considered so far, i.e. RC circuit and single compartment neuron
146 model, in a major aspect: they can have complex morphologies, where the membrane potential varies between different
147 compartments and membrane capacitance is distributed across the neuronal structure. As the CapClamp in contrast
148 operates locally through the recording electrode, the emulated capacitance change is expected to be localized to the
149 recorded compartment instead of affecting all compartments (see Methods). To demonstrate such localized capacitance
150 changes and study their effects on neuronal spiking, we applied the CapClamp in *in vitro* patch-clamp recordings of rat
151 dentate gyrus granule cells (DGGCs). Among morphologically complex cells, DGGCs appear well-suited to test the
152 CapClamp, because their morphological structure, consisting of a central soma and one to four primary apical dendrites
153 as shown in Figure 3 A [24], translates to a relatively compact electrotonic structure [25, 26].

154 **2.4.1 Measurement of local near-somatic capacitance**

155 Most capacitance measurements aim to provide an accurate estimate of the *global* capacitance of a neuron [1, 2]. To
156 correctly infer the transmembrane and axial current, however, the CapClamp requires the *local* capacitance value of the
157 compartment where the electrode is placed at. For the somatic DGGC recordings, we exploit that the current clamp step
158 method – fitting charging curves via a sum of exponential terms – can also provide local capacitance information [1].
159 DGGC charging curves consisted of a slow (τ_0 : 15.1 ± 4.8 ms, R_0 : 127 ± 45 M Ω) and a fast (τ_1 : 0.77 ± 0.24 ms, R_1 :
160 35 ± 15 M Ω) component. Such a response can be understood in terms of a two compartment circuit consisting of a
161 *near* compartment, comprising the patched soma and its surrounding, coupled to a *far*, mostly dendritic, compartment
162 as depicted in Figure 3 A (for details on the mapping, see Methods). Importantly, the slow and fast components
163 can be mapped to the corresponding five circuit parameters: near capacitance C_n (21.0 ± 9.4 pF), near resistance
164 R_n (854 ± 394 M Ω), coupling resistance R_a (53 ± 20 M Ω), far capacitance C_f (106 ± 33 pF) and far resistance R_f
165 (156 ± 60 M Ω)(Fig. 3 C). Accordingly, this near-somatic capacitance C_n represents the summed capacitance of the
166 membrane area that is electrotonically close to the recording site and thus is the value that the CapClamp requires as
167 input and should be able to modify.

168 **2.4.2 Altered near-somatic capacitance in DGGCs**

169 To confirm the localized effect of the CapClamp, we repeated the above capacitance measurement while clamping
170 DGGCs at values ranging from 0.6 to 3 times the original near capacitance. Figure 3 B depicts how the charging of the
171 membrane potential in an exemplary cell changed its shape in reaction to the clamp. Both slow and fast time constant
172 lengthened with capacitances, whereas the associated resistances increased and decreased, respectively, such that their
173 sum, the total input resistance (which is expected to be independent of capacitance), remained constant. These measured
174 time constants and amplitudes matched the predicted ones for a two compartment circuit with a near capacitance at the
175 chosen target values and all other circuit parameters at their original values. In a multicompartment simulation of a

176 morphologically reconstructed DGGC, we could reproduce both the two compartment structure of DGGCs and the
177 isolated modification of the near capacitance, further confirming the local control via the CapClamp.

178 Across 18 recorded cells, the CapClamp robustly altered DGGC charging curves and allowed to modify the charging
179 time constants. Within the tested capacitance range, the slow time constant τ_0 decreased by -0.8 (-1.0 to -0.6) ms,
180 median and interquartile range in parentheses, and increased up to 3.0 (2.4 to 3.9) ms, whereas the fast time constant
181 τ_1 changes ranged from -0.24 (-0.29 to -0.20) ms up to 0.60 (0.36 to 0.86) ms (Fig. 3 D). To quantify how well these
182 changes reflected an altered near capacitance, we evaluated the goodness of fit between the observed and expected time
183 constants and resistances. In the majority of cells, R-squared values were close to 1, indicating that the CapClamp
184 induced the expected changes (τ_0 : 0.87 (0.76 to 0.92), R_0 : 0.77 (0.56 to 0.89), τ_1 : 0.76 (0.32 to 0.97), R_1 : 0.85
185 (0.75 to 0.91)). The largest mismatches occurred for the fast time constant, especially at high capacitances, where the
186 measured time constant was often shorter than predicted (Fig. 3 D). A small bias towards a shorter fast component is
187 to be expected and also present in the multicompartment simulation, because this time constant was only about ten
188 times longer than the recording interval of 50 μ s limiting its slow-down by the CapClamp currents. Larger deviations of
189 τ_1 however could not be reproduced in numerical simulations and likely result from other error sources, such as the
190 difficulty of fitting this small and short time constant in the presence of noise or imprecise estimates of the original near
191 capacitance (see Methods). Overall, in terms of circuit parameters, the capacitance measurements overall confirmed
192 the targeted near capacitance change for 12 out of 18 cells within an average error of 10% (Fig. 3 E). Concluding, the
193 CapClamp achieved an isolated change of the near-somatic capacitance in DGGCs and thereby allows to control the
194 time constants of their passive voltage dynamics.

195 **2.4.3 Near-somatic capacitance governs action potential shape and firing frequency in dentate gyrus granule** 196 **cells**

197 In neurons such as the recorded DGGCs, where the axon directly emerges from the soma, the ability to clamp the
198 near-somatic capacitance provides control over the major capacitive load for the action potential generating site in
199 the axon initial segment. Consequently, the CapClamp, although acting locally, is expected to impact action potential
200 (AP) dynamics and excitability of a morphologically complex DGGC as demonstrated earlier for the simplified single-
201 compartment neuron model (Fig. 2). To illustrate how the CapClamp can thus be applied as a novel probe to
202 characterize neuronal firing, we compared spiking responses and f-I curves across near capacitances ranging from 0.6
203 to 3 times the original value, corresponding to a range from 10 pF to 60 pF.

204 Clamping the near-somatic capacitance in DGGCs, we observed pronounced changes in the spiking response to
205 depolarizing current step, clearly visible in the raw voltage traces (Fig. 4 A). The most apparent change was an altered
206 AP shape (Fig. 4 B) – a continuous reduction of AP peak amplitude (from 61 ± 9 mV at $0.6 C_n$ to 24 ± 16 mV at
207 $3 C_n$) and a simultaneous broadening of AP width (from 0.75 ± 0.15 ms at $0.6 C_n$ to 1.30 ± 0.40 ms at $3 C_n$) with
208 increasing capacitance (Fig. 4 C and D). In addition, fast afterhyperpolarization (fAHP) was diminished and disappeared
209 in the majority of cells after increasing capacitance (fAHP in 9/10 cells at $0.6 C_n$ and 2/10 at $3 C_n$). Importantly, the

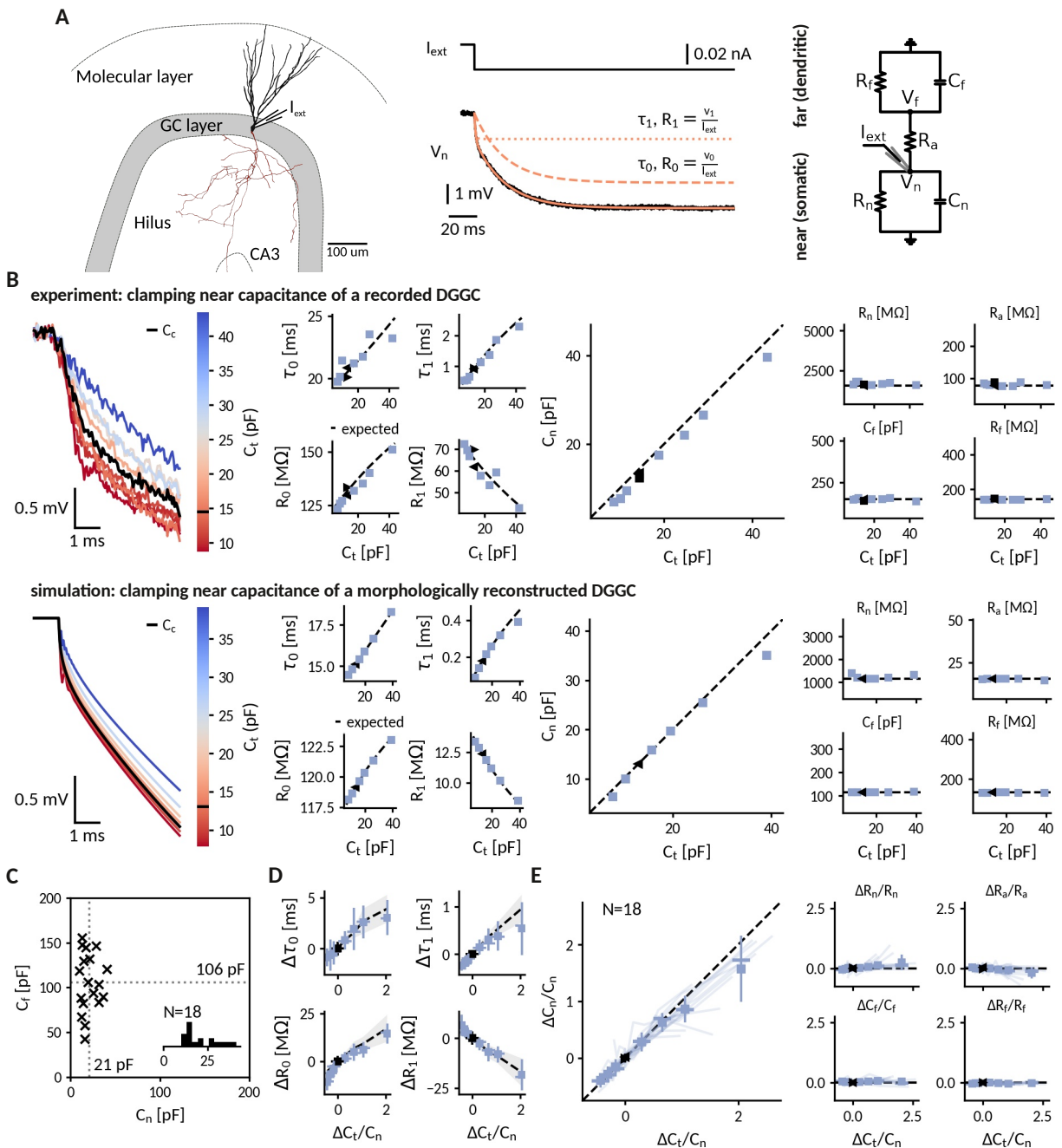


Figure 3: Clamping capacitance in rat dentate gyrus granule cells. **A** Morphology of a DGGC (left) and response to a hyperpolarizing current injected at the soma, fit via a sum of exponential terms with a slow τ_0 , v_0 and a fast component τ_1 , v_1 (middle), which can be mapped to two resistively coupled RC-circuits (right) with a near (somatic) compartment C_n and R_n , resistive coupling R_a and a far (dendritic) compartment C_f and R_f . **B** *Left*: Voltage responses of a recorded (top) and a simulated morphologically-reconstructed (bottom) DGGC to a current pulse (exp: -27 pA, sim: -50 pA) clamped at 0.6- to 3-fold the cell's near capacitance (black: original, color: target near capacitances). *Middle*: Slow and fast components versus target capacitance. *Right*: Circuit parameters versus target capacitance. \blacktriangleleft , \blacktriangleright : before and after clamping, blue square: clamped, dashed line: expected values. **C** Measured near C_n and far C_f capacitances for 18 DGGCs (gray dotted: mean). Inset: histogram of near capacitances. **D** Changes of slow and fast components in all recorded cells versus relative targeted change of near capacitance (squares: mean, horizontal line: median, vertical line: std, shaded area: std of expected changes). **E** Relative changes of circuit parameters versus relative targeted change of near capacitance. Legend same as in **D** and individual cells shown with transparent blue lines.

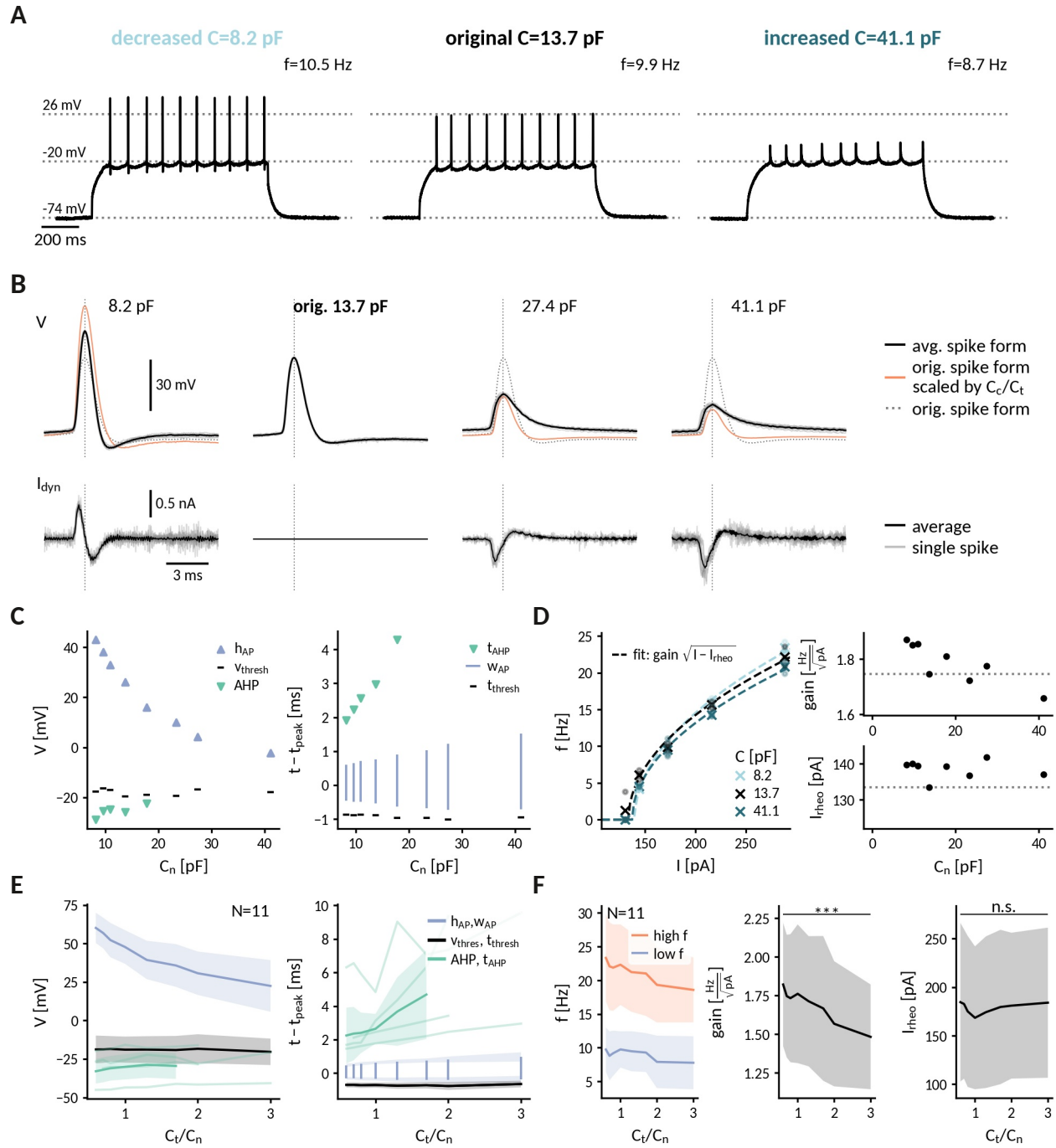


Figure 4: Repetitive spiking and action potential shapes in DGGCs clamped at different capacitances. **A** Spiking at decreased 0.6-fold (left), original (middle) and increased 3-fold (right) near capacitance C_n . **B** Spike shapes (top) and capacitance clamp currents (bottom) for increasing capacitances from 0.6 to 3-fold of the original near capacitance (black: mean, light gray: single spikes, orange: expected spike shape for unaltered intrinsic currents, dotted: spike shape at original capacitance). **C** Comparison of spike shape (left) and temporal structure (right) across tested near capacitances. **D** Measured f - I at 0.6, 1 and 3-fold near capacitance with fit $f = gain \sqrt{I - I_{rheo}}$ (dashed lines). Extracted gain and rheobase for all tested near capacitances (dotted line: values at original capacitance 13.7 pF). **E** Effect of capacitance changes on spike shape (left) and temporal structure (right) for all recorded DGGCs (solid: mean, shaded: std). To compare different cells, the capacitance is shown relative to the original near capacitance and spikes were compared at 1.2 fold of the cell's rheobase. **F** Effect of capacitance changes on firing frequency, low firing (blue) at 1.2 fold rheobase and high firing (red) at 2.0 fold rheobase (left), gain (middle) and rheobase (right) for all recorded DGGCs (solid: mean, shaded: std).

210 observed disappearance of fAHP cannot be explained by increased capacitive filtering alone, which would decrease
211 the its amplitude, but cannot abolish it. It thus demonstrates that the somatic capacitive load in DGGCs is able to
212 influence the AP generating currents.

213 To illustrate the interplay of capacitance and the AP generating currents, we compared the observed spikes with
214 hypothetical ones obtained by assuming unaltered currents with respect to the original capacitance (see Methods).
215 Recorded and hypothetical spike shapes exhibited marked differences (Fig. 4 B). At 0.6-fold decreased capacitances,
216 for example, the recorded AP amplitude was significantly smaller than the hypothetical one (rec.: 61 ± 9 mV, hyp.: 95
217 ± 18 mV, Wilcoxon signed-rank $p < 0.001$), presumably reflecting a reduction of the driving force for the sodium current
218 when the AP peak approaches the reversal potential of sodium. Furthermore, at 3-fold increased capacitance, as noted
219 above the recorded spikes exhibited no fAHP in most cells while the hypothetical ones still did (fAHP rec: 2/10, hyp:
220 10/10) – potentially a result of a reduced activation of potassium channels due to lower AP amplitudes and/or earlier
221 closing during the slowed AP repolarization. In contrast to driving force and gating dynamics, the channel kinetics,
222 e.g. their activation curves, cannot be altered by capacitance. Correspondingly, the spike threshold, which reflects the
223 voltage where sodium channels start to massively open, was not significantly correlated with near capacitance (Pearson
224 correlation $r = 0.089$, $p = 0.42$). Taken together, our analysis indicates that an altered somatic capacitance affects both
225 sodium and potassium currents in DGGCs.

226 Controlling the spike initiation zone, near-somatic capacitance also governed DGGC excitability. With increasing
227 capacitance, DGGCs became less excitable and firing frequencies significantly decreased (Fig. 4 D and F). From 0.6- to
228 3-fold of the original near capacitance, the decrease was modest for low firing rates close to threshold (from 9.2 ± 3.6
229 Hz to 7.6 ± 3.7 Hz, Wilcoxon signed-rank $Z = 47$, $p = 0.024$) and became more pronounced for high firing rates at the
230 largest injected currents (from 22.2 ± 7.0 Hz to 17.9 ± 5.1 Hz, $Z = 55$, $p = 0.001$). In this respect, the firing rate-current
231 (fI) curves of the DGGCs resembled those obtained for the simulated neuron (compare Fig. 2 D): the gain decreased for
232 increased capacitances (from 1.74 ± 0.45 Hz/ $\sqrt{\text{pA}}$ at $0.6 C_n$ to 1.42 ± 0.37 Hz/ $\sqrt{\text{pA}}$ at $3 C_n$, $Z = 55$, $p = 0.001$), but the
233 rheobase current remained relatively constant (from 182 ± 77 pA at $0.6 C_n$ to 179 ± 75 pA at $3 C_n$, $Z = 12$, $p = 0.13$).
234 Overall, we conclude that a change of the near-somatic capacitance alone was sufficient to modify the input-output
235 relationship of the recorded DGGCs.

236 2.5 Applications of the CapClamp

237 The CapClamp lends itself to either test hypotheses on the impact of capacitance or to exploit the control over the
238 membrane time constant in order to to alter neuronal dynamics in informative ways. In the following, we briefly
239 illustrate use cases of the CapClamp from these two fields, applying the technique to experimentally explore effects of
240 capacitance on temporal integration, energetic costs of spiking and bifurcations.

241 **2.5.1 Temporal integration**

242 A basic processing step in neuronal computation is temporal integration, the summation of time-separated synaptic
243 inputs [27, 28]. An upper limit for temporal integration, at least in the absence of dedicated active channels, is set by
244 the membrane time constant $\tau = RC$, which is directly proportional to the cell's capacitance. Hence, increasing the
245 capacitance of a cell should make it a better integrator: if two inputs arrive separated in time, the cell's response to
246 the second one should be higher than to the first one. Indeed, when we compared the responses of DGGCs to current
247 pulse trains with different interstimulus intervals (ISI) clamped at decreased and increased near-somatic capacitances, a
248 capacitance increase allowed the cell to better “sum” pulses at an ISI of 5 ms as apparent by the larger step sizes in
249 the stair-like voltage response and the finally higher ratio of last to first pulse response. (Fig. 5 B). At an ISI of 50
250 ms, in contrast, neither capacitance allowed temporal integration. The biological relevance of tailoring capacitance
251 to temporal processing can, for example, be observed in auditory cells of the barn-owl, which have no dendrites to
252 reduce capacitive and resistive load and hence shorten their time constant such that they can perform sub-millisecond
253 coincidence detection [29].

254 **2.5.2 Energy consumption during spiking**

255 Action potentials are energetically expensive, because the required sodium and potassium ions have to be pumped back
256 using ATP [20, 30]. The minimal amount of ionic charge required for an action potential is dictated by the capacitance
257 as $Q = C\Delta V_{AP}$, suggesting that a smaller capacitance is energetically favorable. In order to gauge how capacitance
258 affects charge deposit and energy consumption, we reexamined spike shapes for a fixed current input at different
259 capacitances both in the simulated neuron and in the recorded DGGCs (Fig. 5 C and E). We found that despite a reduced
260 amplitude at higher capacitances, these smaller spikes still required more depolarizing charge $Q_+ = C\Delta V_{AP}$ (Fig. 5
261 D and F). In the model, we tested whether this depolarizing charge provided a reliable indication of the sodium charge
262 Q_{Na^+} , which finally determines pump activity and energy consumption (Fig. 5 D). The sodium charge exceeded the
263 depolarizing charge, because sodium and potassium currents temporally overlap, but it increased in a similar manner
264 with capacitance. Taken together, in the tested model and the recorded DGGCs, energy consumption per action potential
265 appears to be reduced at smaller capacitances. In line with this observation, it has been reported that perineuronal nets
266 could decrease membrane capacitance of fast-spiking interneurons, thereby facilitating high-frequency firing, while
267 keeping energetic costs at bay [31].

268 **2.5.3 Neuronal bifurcations**

269 To optimally support neural processing, nerve cells exhibit qualitatively different response properties, which in some
270 cases can be flexibly adapted to context. For example, neurons with class 2 firing (non-zero minimum frequency) can be
271 switched to class 1 firing (arbitrarily low frequency) via neuromodulation [32, 33], transforming them from resonators
272 to integrators. These qualitative differences in response and processing properties are linked to distinct spike generation
273 mechanisms, whose corresponding excitability classes – as well as transitions between them – can be characterized

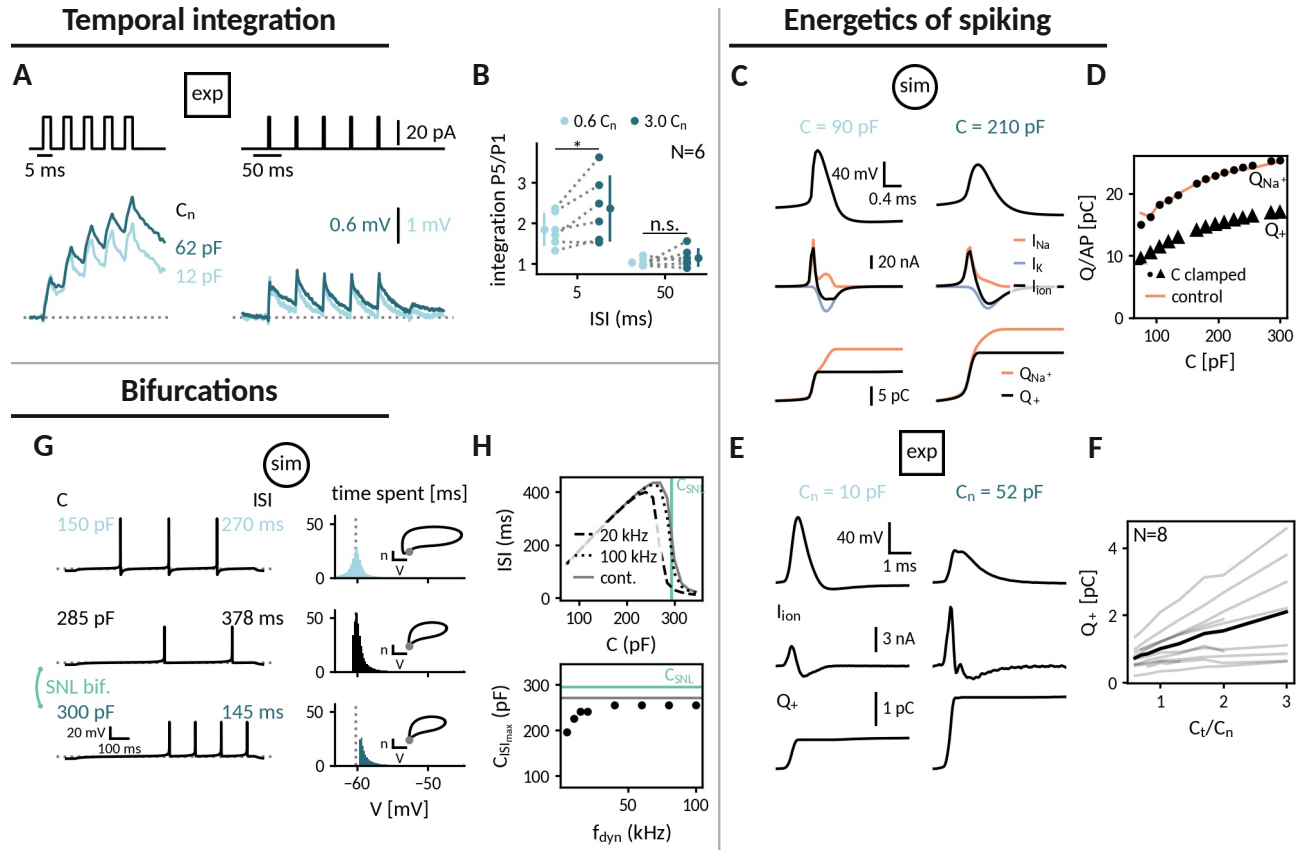


Figure 5: Applying the capacitance clamp to study neuronal signalling and physiology. Temporal integration: **A** Current pulses with interstimulus intervals of 5 ms and 50 ms (top) and voltage responses of an exemplary DGGC at a decreased (12 pF) and an increased (62 pF) near capacitance (voltage scale adapted to first response height). **B** Ratio of fifth and first response as a measure of temporal integration for a 0.6-fold decreased capacitance in comparison to a 3-fold decreased one at 5 ms and 50 ms ISI. **Energetics of spiking:** **C** Spike shape (top), sodium, potassium and total ionic current (middle) and deposited sodium Q_{Na^+} as well as depolarizing Q_+ charge (bottom) in the Wang-Buzsaki neuron model for a 90 pF and a 210 pF capacitance. **D** Sodium Q_{Na^+} and depolarizing Q_+ charge per action potential versus capacitance (original: 150 pF, clamped: dot and triangle, control: gray). **E** Spike shape and depolarizing charge for a dentate gyrus granule cell clamped at decreased 10 pF and increased 52 pF capacitance. **F** Deposited depolarizing charge versus relative change of near capacitance in recorded DGGCs (black: mean, gray: individual cells). **Studying bifurcations:** **G Left:** In the Wang-Buzsaki neuron model, spiking slows down when increasing capacitance up to 285 pF, but a further small increase to 300 pF abruptly doubles the firing frequency, a signature of a saddle-node-loop (SNL) bifurcation. **Right:** Histograms of the time spent at different membrane potentials between two spikes. Insets show the spike dynamics in the potassium gating n -voltage V plane. **H Top:** Interspike interval against capacitance for simulated capacitance clamps at 20 kHz (dashed) and 100 kHz (dotted) dynamic clamp frequency versus the control simulation (gray) with indication of the expected critical capacitance C_{SNL} (green). **Bottom:** Capacitance at maximal ISI against dynamic clamp frequency.

274 by bifurcation analysis [34, 35]. Prior work recently highlighted the *saddle-node loop* (SNL) bifurcation, because it
275 separates firing regimes with drastic differences in synchronization and can be induced by a wide array of physiological
276 parameters, including temperature and extracellular potassium, as well as capacitance [13, 14]. We chose this transition
277 and asked whether the CapClamp can correctly locate the SNL bifurcation and, therefore, provide an estimate where a
278 neuron “positions itself” with respect to this critical switch.

279 To detect the SNL bifurcation in capacitance space, we looked for one of its footprints: frequency-doubling, a drastic
280 increase of frequency for an incremental capacitance increase. In the simulated neuron, testing capacitances from 150 pF
281 up to 285 pF, the neuron fires at ever slower rates, but at 300 pF, the neuron indeed abruptly doubles its firing rate (Fig. 5
282 G). At this capacitance, the neuron fires faster, because the modified action potential switches to a trajectory, where
283 it skips one half of the slow recharging after a spike (see the voltage histograms in Fig. 5 G). In the simulations, the
284 CapClamp reproduced this frequency-doubling and, given a sufficiently fast dynamic clamp (>40 kHz), also correctly
285 located the critical capacitance where the SNL bifurcations occurs (Fig. 5 H). In the recorded DGGCs, we found no
286 evidence of frequency doubling in the tested capacitance range (Fig. 4 D and F), indicating that the DGGCs are at a
287 point in capacitance space further away from the SNL bifurcation.

288 **3 Discussion**

289 The dynamic clamp is a valuable tool in intracellular recordings to examine the diverse roles of ionic conductances in
290 excitable cells [9, 15, 16, 36]. In this study, we introduced the capacitance clamp (CapClamp), an application of the
291 dynamic clamp that allows to mimic a modified membrane capacitance in a biological neuron. Via simulations of a
292 biophysical neuron model, we confirmed that the CapClamp correctly captures how capacitance affects spike shapes and
293 firing frequency. In recordings of rat dentate gyrus granule cells, we further verified that the CapClamp could accurately
294 control the capacitance of the recorded somatic compartments. Moreover, we clamped this near-somatic capacitance of
295 DGGCs during spiking and found that, as predicted by our simulations, capacitance can modify the fI curve and alter
296 the course of the spike generating currents. CapClamp can serve as a new probe to neuronal signaling, physiology and
297 bifurcations. In the following, we highlight requirements for the CapClamp and discuss how this experimental control
298 over capacitance can benefit the study of cellular electrical behavior.

299 **3.1 Precise, flexible and local control over capacitance in all excitable cells**

300 To our knowledge, the CapClamp is the first tool to experimentally study capacitance changes in a precise and flexible
301 manner. The CapClamp owes its precision and flexibility to the virtual nature of the altered capacitance. In contrast,
302 methods to physically modify the capacitance are affected by various undesired side effects. Dendritic pinching,
303 decoupling dendrites from the soma, for instance greatly reduces membrane area and thereby capacitance, but also
304 removes all dendritic conductances [37]. Capacitance alterations have also been reported after application of mefloquine,
305 a drug binding to membrane phospholipids, but it also blocks gap junctions [38]. A notable exception is the recent

306 demonstration of engineered polymer synthesis in neuronal cell membranes, which alters their capacitance, but not their
307 input resistance [39]. In comparison, however, the CapClamp provides provides more accurate and dynamic control
308 by allowing to test multiple selected capacitance values in a single cell (Fig. 3 and Fig. 4), while being significantly
309 simpler to implement.

310 The CapClamp can be applied in every excitable cell. Here, we focused on neurons, but the proposed clamping currents
311 can also be used to study capacitance changes in other cells, including for example heart cells [36, 40]. In particular,
312 no prior knowledge about the ionic or external currents in the clamped cell is required, so that the capacitance can be
313 clamped during any experimental (step current, ramp current, etc.) or during synaptic input. Furthermore, capacitance
314 can be clamped in both electrotonically compact cells like oocytes [41] and non-compact cells like most neurons [26],
315 although in the latter case the CapClamp is limited locally to the capacitance of the recorded compartment (Fig. 3).
316 Consequently, the effects of clamping capacitance depend on the recording site and the cell's morphology. The soma, for
317 example, represents the major capacitive load for spike generation in vertebrate neurons, where the axon predominantly
318 emerges close to the soma (Fig. 4), but it is expected to exert less influence in neurons, where the axon comes out of the
319 dendritic tree, a common feature of invertebrate neurons [42].

320 The major prerequisite to apply the CapClamp is a reliable capacitance measurement of the clamped compartment,
321 which can be challenging, especially for electrotonically complex cells [1, 2]. An imprecise capacitance estimate leads
322 to erroneous clamping currents, which increase high frequency noise for small errors and might even induce instabilities
323 for larger errors. The measurement method presented for the recorded DGGCs, i.e. mapping the charging response to a
324 two compartment circuit, could in principle be extended to cells with a larger number of compartments e.g. pyramidal
325 cells [43, 44]. Yet, accurate multi-exponential fitting is demanding and the assumption of uniform membrane properties
326 underlying the mapping is a simplification, shown to be violated in some cells, such as GABAergic interneurons
327 [45]. As an alternative, measurement protocols could be exploited that inherently yield local capacitance estimates,
328 including fast voltage ramps [1] or sampling of voltage responses to fast fluctuating currents [46]. Reliable capacitance
329 measurements further allow to compare measured and target capacitance of the clamped cell, which serves as a first
330 simple test to ensure the quality of the CapClamp.

331 **3.2 A CapClamp on every rig**

332 As a novel application of the established dynamic clamp technique, the CapClamp is an accessible and low-cost
333 extension of a standard electrophysiology stack [15, 16]. For an existing dynamic clamp setup, the sole requirement is
334 to implement the calculation of the clamping currents (see Eq. 5). Otherwise, multiple open source frameworks exist
335 that only require a dedicated computer with a data acquisition card to enable the dynamic clamp in a conventional
336 electrophysiology setup [47–53]. To facilitate the usage of the technique, we provide code for the CapClamp scheme in
337 the RELACS and RTXI frameworks (see Appendix).

338 In CapClamp recordings, as in all dynamic clamp applications, a high sampling frequency and accurate voltage
339 monitoring are key [54]. Whether a sampling frequency is sufficiently high can be tested by assuring that the observed
340 voltage dynamics e.g. the spike amplitudes are invariant when the sampling frequency is decreased from the maximal
341 possible value [8]. For the simulated fast-spiking interneuron, we found a satisfactory clamp at a frequency of 20 kHz,
342 which we expect to also be sufficient for most excitatory neurons, because they tend to have slower voltage dynamics
343 [20]. In our single electrode recordings, we focused on careful electrode compensation to avoid electrode artifacts in
344 the recorded voltages which would lead to incorrectly estimated membrane currents and eventually instabilities. To
345 improve voltage monitoring, future applications could either apply active electrode compensation [55, 56] or resort to
346 two electrode recordings, where current injection and voltage recordings are separated.

347 **3.3 Modifying capacitance as a probe for cellular electrical dynamics**

348 Via the CapClamp, experimenters can ask a question that was previously accessible only in theoretical work: What if
349 capacitance was different? In contrast to the theoretical approach, the answers to this question do not have to rely on
350 models of channel dynamics or other membrane properties, because the latter are provided by the biological cell itself
351 [9]. Modifying capacitance with the CapClamp can serve either to investigate changes in this biophysical parameter or,
352 more broadly, to alter the membrane time constant of a cell as a way to characterize its electrical dynamics.

353 **3.3.1 Understanding the role of capacitance**

354 The virtual capacitance changes induced by the CapClamp could serve to address two crucial questions about actual
355 membrane biophysics: why capacitance appears to be biologically mostly constant [3] and how exceptions to this rule
356 can facilitate or deter neuronal function [4, 6, 31, 57]. Capacitance is for example rarely tested for optimality - a common
357 question in ion channel kinetics, which appear optimized for function and energy expenditure [20, 58]. Regarding
358 energy consumption, our CapClamp experiments in DGGCs indicate that action potentials become energetically cheaper
359 at lower capacitances (Fig. 5 E and F). Interestingly, reports of exceptional capacitance values mostly find reductions
360 e.g. for myelinated axons ($C_m \approx 0.05$ uF/cm² for a ten-fold wrapped myelin sheath, see [59]) or human pyramidal cells
361 ($C_m \approx 0.5$ uF/cm², see [6]) suggesting that indeed the metabolic cost of AP generation could have been a contributing
362 factor to capacitance adaptations. Moreover, the recent hypothesis that perineuronal nets can reduce capacitance of
363 interneurons in a similar way as myelination of axons suggests that capacitance adaptation could be more widespread in
364 the brain than often assumed [31].

365 **3.3.2 Altering the membrane time constant**

366 A key contribution of the CapClamp is the isolated experimental control of the membrane time constant. Monitoring how
367 the membrane potential dynamics change in response to such a perturbation of the time constant has been a theoretical
368 tool to characterize a cell's electrical behavior [11, 13]. As an experimental analogue, the CapClamp could for example
369 be used to further constrain and improve fitting of conductance-based neuron models [11, 60, 61]. Furthermore, the

370 CapClamp can be used to identify capacitance values where qualitative changes of activity occur (bifurcations, see
371 Fig. 5 G and H), such as a switch to bistable firing [13, 14]. If a neuron is found to be close in capacitance/membrane
372 time constant space to such a critical switch, this can have important implications for infrared [62, 63] and ultrasonic
373 [64, 65] stimulation of neural activity, whose effects are assumed to rely on rapid alteration of the capacitance, as well
374 as for other perturbations such as changes of temperature [13] or extracellular potassium [14], which have similar
375 temporal effects as capacitance. Finally, the broad impact of the time constant on firing frequency and spike shape could
376 be used to examine activity-dependent physiological processes such as ion concentration dynamics [14] or calcium
377 controlled channel homeostasis [66–68].

378 **3.4 Conclusion**

379 Taken together, the presented CapClamp enables an accurate and flexible control over capacitance in biological neurons,
380 a basic determinant of cellular excitability, that so far has been inaccessible in experiment. We expect that the CapClamp
381 will, therefore, broaden and enrich the electrophysiological study of neurons and other excitable cells. With expanding
382 techniques to sense and manipulate neural activity, the combination of modeling and targeted closed-loop feedback that
383 underlies the CapClamp (and more generally the dynamic clamp [69]) will further unlock experimental control over
384 other previously inaccessible aspects of single neuron [70–72] and network dynamics [73, 74].

385 4 Materials and Methods

386 4.1 Derivation of the CapClamp current

In order to derive a dynamic clamp feedback scheme for the CapClamp, we compare the actual membrane potential dynamics at the original capacitance C_c with the target dynamics at the chosen capacitance C_t . The actual dynamics of the cell, which for the moment is assumed to be isopotential, is given by the current-balance equation of a single compartment

$$\frac{dV}{dt} = \frac{I(V, t) + I_{dyn}(t)}{C_c}, \quad (2)$$

with capacitance C_c , membrane currents $I(V, t)$ (comprising all ionic and synaptic currents, as well as external stimuli) and the dynamic clamp current $I_{dyn}(t)$. Note that ionic and synaptic contributions to the membrane currents $I(V, t)$ are voltage-dependent, both with respect to driving force and gating dynamics, so that a voltage trajectory governed by a different capacitance also leads to a modified shape of the membrane currents. In the target dynamics, the dynamic clamp current is absent and the capacitance is modified to the desired value

$$\frac{dV}{dt} = \frac{I(V, t)}{C_t}. \quad (3)$$

Both membrane potential trajectories would coincide, if we chose a dynamic clamp current such that the right-hand sides of actual (Eq. 2) and target dynamics (Eq. 3) become identical,

$$I_{dyn}(t) = \frac{C_c - C_t}{C_t} I(V, t).$$

Generally, an exact model for the membrane currents $I(V, t)$ will not be available, as it would require knowledge about all active conductances and incoming synaptic inputs. Instead, the membrane current can be estimated from the stream of incoming voltage data using the discrete version of Equation 2

$$I(V_{i-1}, t_{i-1}) \approx C_c \frac{V_i - V_{i-1}}{\Delta t} - I_{dyn, i-1} \quad (4)$$

387 where Δt is the sampling interval¹. A prerequisite is the measurement of the cell capacitance C_c . Furthermore, for
388 the estimation to be accurate, the sampling interval needs to be shorter than the fastest time scales of changes in the

¹The indexing in Equation 5 assumes a voltage sampling $V_i = V(i\Delta t)$ and a current injection $I_{dyn, i} = I_{dyn}(i\Delta t)$. However, sampling can take a non-negligible amount of time, so that depending on the sampling system the currently available voltage actually represents the voltage from the previous cycle $V_i = V((i-1)\Delta t)$. In this case, for a correct estimation of the membrane currents, the dynamic clamp current index has to be shifted correspondingly,

$$I_{dyn, i} = \frac{C_c - C_t}{C_t} \left(C_c \frac{V_i - V_{i-1}}{\Delta t} - I_{dyn, i-2} \right).$$

389 membrane currents e.g. sodium gating time constants. With this estimated membrane current, the complete expression
390 for the CapClamp current reads

$$I_{dyn,i} = \frac{C_c - C_t}{C_t} \left(C_c \frac{V_i - V_{i-1}}{\Delta t} - I_{dyn,i-1} \right). \quad (5)$$

391 The above derivation assumes that the cell is isopotential. In the case of an electrotonically non-compact cell, the steps
392 are identical, but the cell capacitance C_c has to be replaced by the capacitance of the compartment where the recording
393 electrode is located. Consequently, in a non-isopotential neuron, the mimicked capacitance modification is restricted
394 to the compartment at the tip of the recording electrode - a constraint known as the space clamp that is shared by all
395 clamping techniques [15, 75].

396 4.2 Capacitance measurements

To apply the CapClamp, a prerequisite is to measure the capacitance of the recorded local compartment. Here, we use
the current clamp protocol, which estimates the capacitance from the voltage response to a current step with amplitude
 I_{ext} ,

$$V(t) = \sum_i v_i \left(1 - e^{-\frac{t}{\tau_i}} \right) = I_{ext} \sum_i R_i \left(1 - e^{-\frac{t}{\tau_i}} \right), \quad (6)$$

397 where an ordering in terms of these time scales is assumed i.e. $\tau_0 > \tau_1 > \dots$. Depending on the morphology, this
398 sum can have a large number of components [76], but in practice often only two or three components can be reliably
399 extracted. As described in Golowasch et al. [1], the slowest component τ_0 is the membrane time constant and allows to
400 infer the total capacitance of a neuron by $C = \frac{\tau_0}{R_0} = \frac{\tau_0}{v_0} I_{ext}$. In the case of an isopotential cell, the membrane time
401 constant is the only component in the charging curve and the total capacitance can be used for the CapClamp.

402 4.2.1 Measurement of near capacitance

For the case of two components τ_0, R_0 and τ_1, R_1 in the charging curve (Eq. 6), an equivalent two compartment circuit
can be identified comprising a near compartment with capacitance C_n and resistance R_n connected via a coupling
resistance R_a to a far compartment with capacitance C_f and resistance R_f [1, Appendix A]. With the additional
assumption of a uniform membrane time constant $\tau_m = R_n C_n = R_f C_f$, the fitted two components can be mapped
to the values of these five circuit parameters, which in particular provides the near capacitance C_n required for the
CapClamp (for the full mapping see [Appendix][Mapping a charging curve with two components to a two compartment
circuit])

$$C_n = \frac{\tau_0 \tau_1}{\tau_1 R_0 + \tau_0 R_1}. \quad (7)$$

403 When the capacitance is subsequently clamped to a k-fold different value, $C_t = k C_n$, the uniformity assumption has to
404 be correspondingly adjusted to $R_n C_n = k R_f C_f$.

405 **4.3 CapClamp in dentate gyrus granule cells**

406 **4.3.1 Electrophysiology**

407 Acute brain slices were produced as described earlier [77]. Briefly, rats were anesthetized (3% Isoflurane, Abbott,
408 Wiesbaden, Germany) and then decapitated. Brains were removed quickly and transferred to carbogenated (95% O₂ /
409 5% CO₂) ice-cold sucrose-ACSF containing (in mM): 87 NaCl, 2.5 KCl, 25 NaHCO₃, 1.25 NaH₂PO₄, 25 glucose,
410 75 sucrose, 7 MgCl₂, 0.5 CaCl₂, 1 Na-pyruvate, 1 ascorbic acid. Horizontal brain slices of 300 μm thickness were cut
411 using a Vibratome (VT1200 S, Leica, Wetzlar, Germany). Hippocampal tissue slices, were collected and placed in
412 a submerged holding chamber filled with carbogenated sucrose ACSF at 32–34 °C for 30 minutes and then at room
413 temperature for 15 minutes before recording. Experiments were alternated between left and right hemisphere slices to
414 prevent bias due to slice condition.

415 For recording, slices were transferred to a submerged chamber and superfused with pre-warmed, carbogenated ACSF
416 containing (in mM): 125 NaCl, 2.5 KCl, 25 NaHCO₃, 1.25 NaH₂PO₄, 25 glucose, 1 MgCl₂, 2 CaCl₂, 1 Na-pyruvate,
417 1 ascorbic acid. The bath temperature was set to 32–34 °C with a perfusion rate of 12–13 ml/min. Slices were
418 visualized using an upright microscope (AxioScope; Zeiss) equipped with infrared differential interference contrast optics
419 and a digital camera (Retiga EX QImaging CCD, Teledyne Photometrics, AZ, USA). Granule cells from the DG were
420 chosen based on their anatomical location within the hilus as well as their morphological appearance.

421 Whole-cell patch-clamp electrodes were produced from borosilicate glass capillaries (outer diameter 2 mm, inner
422 diameter 1 mm, Hilgenberg, Germany) using a horizontal puller (P-97, Sutter Instruments, CA, USA) and filled with an
423 intracellular solution consisting of (in mM): K-gluconate 130, KCl 10, HEPES 10, EGTA 10, MgCl₂ 2, Na₂ATP 2,
424 Na₂GTP 0.3, Na₂Creatine 1 and 0.1% biocytin (adjusted to pH 7.3 and 315 mOsm), giving a series resistance of
425 2.5–4 MΩ. All recordings were performed with a SEC LX10 amplifier (npi electronic, Germany), filtered online at
426 20 kHz with the built-in Bessel filter, and digitized at 20 kHz (National Instruments, UK). Following breakthrough into
427 whole-cell configuration, we adjusted the bridge and capacitance compensation before switching to the dynamic clamp
428 mode for recording. Cells were excluded if resting membrane potential was more depolarized than –45 mV. The liquid
429 junction potential was not corrected.

430 **Neuronal visualization and immunohistochemistry** Following recording, selected cells were immersion fixed in 4%
431 paraformaldehyde (PFA) in 0.1 M phosphate buffer (PB, pH 7.4) at 4°C for 24 - 48 hours, slices were then transferred
432 to fresh PB. Prior to immunohistochemical processing, slices were rinsed in PB, followed by PB buffered saline (PBS,
433 0.9% NaCl). Slices were then rinsed in PBS and incubated in a fluorescent-conjugated streptavidin (Alexa Fluor-647,
434 1:1000, Invitrogen, UK) in PBS solution containing 3% NGS, 0.1% TritonX-100 and 0.05% NaN₃ for 24 hours at 4°C.
435 Slices were rinsed in PBS and then desalted in PB before being mounted (Fluoromount-G, Southern Biotech) on 300
436 μm thick metal spacers, cover-slipped, sealed, and stored at 4°C prior to imaging.

437 **Confocal imaging and reconstruction** DGGCs were imaged on a laser scanning confocal microscope (FV1000,
438 Olympus, Japan). First, a low magnification (4x air immersion, Olympus, Japan) overview image was taken to confirm
439 the cellular type and localization to the DG, then high resolution z-stacks were made with a 30x silicone immersion
440 lens (N.A. 1.05, UPlanSApo, Olympus) over the whole extent of the cell (1 μm axial steps). Images were reconstructed
441 offline using the FIJI software package (imagej.net) and Neutube (neutracing.com)[78]. Image stacks were stitched in
442 FIJI, then the cells were reconstructed and volume filled using Neutube.

443 **Dynamic clamp setup** Data acquisition and dynamic clamp loop were controlled by RELACS, V0.9.8,
444 RRID:SCR_017280 using a dedicated computer with a Linux-based real time operating system (rtai.org). The sampling
445 frequency was set to 20 kHz and the recordings were performed in discontinuous current clamp with a duty time of
446 16.5 μs . We implemented a CapClamp procedure for RELACS that allows the user to online specify the measured
447 capacitance C_c and the desired target capacitance C_t (for documentation and install instruction see Appendix).

448 **4.3.2 Online measurement of capacitance**

449 For the online measurement of the local capacitance, DGGCs were subjected to twenty hyperpolarizing pulses of
450 200 ms length with 400 ms pauses and an amplitude chosen to produce a response of -5 mV in order to minimize
451 interference from active ionic currents. Responses were averaged and the resulting mean trajectory was fit with a sum
452 of exponentials using the Levenberg-Marquardt method from the python library scipy [79]. Fits were performed with
453 one, two and three components and were compared via the F-statistic [80]. In all recorded DGGCs, the two component
454 fit was significantly better than the one exponential fit ($p < 0.05$, 18/18), whereas no cell exhibited a significant third
455 component ($p < 0.05$, 0/18). Finally, the extracted two components were mapped to a two compartment circuit as
456 explained above and the near capacitance was then used in the subsequent CapClamp.

457 An offline reexamination revealed that in several recorded cells the above fitting procedure yielded inaccurate estimates
458 of the exponential components, e.g. very short fast components due to an artefactual voltage dip *before* pulse onset. To
459 circumvent these problems, improved offline fits were performed for the artifact-free recharging at the pulse end (for
460 more details see Appendix). In 8/18 cells, the offline and the original online estimate of the near capacitance differed
461 by less than 20%, but overall the offline measurement yielded higher capacitance values than originally used for the
462 CapClamp (offline: 21.0 ± 9.4 pF, online: 14.9 ± 4.8 pF). In contrast to the online measurement, the offline procedure
463 reported a better fit with three components for a subset of cells ($p < 0.05$, 7/18), but for the analysis presented here the
464 result of the two component fit is used in all cells.

Table 2: Multi-exponential fit and corresponding circuit parameters in the recorded dentate gyrus granule cells (N=18) and a multicompartment model based on a reconstructed DGGC morphology (see Simulations).

	DGGCs (mean \pm std)	multicomp. model
Exp. fit		
τ_0	15.1 ± 4.8 ms	15.1 ms

	DGGCs (mean \pm std)	multicomp. model
R_0	$127.1 \pm 44.6 \text{ M}\Omega$	$119.2 \text{ M}\Omega$
τ_1	$0.77 \pm 0.24 \text{ ms}$	0.18 ms
R_1	$34.5 \pm 14.7 \text{ M}\Omega$	$12.3 \text{ M}\Omega$
Circuit		
C_n	$21.0 \pm 9.4 \text{ pF}$	13.0 pF
R_n	$854.2 \pm 394.0 \text{ M}\Omega$	$1158.0 \text{ M}\Omega$
R_a	$52.5 \pm 19.8 \text{ M}\Omega$	$15.5 \text{ M}\Omega$
C_f	$105.8 \pm 33.0 \text{ pF}$	113.7 pF
R_f	$155.5 \pm 59.9 \text{ M}\Omega$	$132.8 \text{ M}\Omega$

465 4.3.3 Protocol 1: Verification of altered capacitance

466 After online measurement of the capacitance, each DGGC was clamped at a range of capacitances from 60% to 300%
 467 of the original near capacitance. For each clamped capacitance, the above offline capacitance measurement protocol
 468 was repeated to see how the CapClamp altered the slow and fast components. These time scale and amplitude changes
 469 were then mapped to the corresponding two compartment circuit parameters to compare them to the target capacitance
 470 (see Measurement of near capacitance). Due to the difference between online and offline estimate of the original
 471 near capacitance, we corrected the original target capacitance to $C_t^{\text{corr}} = C_c^{\text{off}} + \Delta C_t$, which preserves the targeted
 472 capacitance change $\Delta C_t = C_t - C_c^{\text{on}}$. Equally, the clamping factors in the mapping were updated to $k = \frac{C_t^{\text{corr}}}{C_c^{\text{off}}}$.

473 4.3.4 Protocol 2: Analysis of fl curves and spike shapes

In a subset of cells, after measuring near capacitance, an fl curve was obtained for the original capacitance and for target
 capacitances in the above range. Current pulses were 1 s long and repeated three times, at amplitudes ranging from 90%
 to 200% of an estimated rheobase. This rheobase was estimated by the first occurrence of spiking in response to a ramp
 (length: 5 s, height: 250 pA). For a quantitative comparison, the resulting fl curves were fit by a square-root function

$$f(I) = \Theta(I - I_{rheo}) \text{gain} \sqrt{I - I_{rheo}}$$

474

475 which captured their type 1 firing with a continuous frequency-current relationship [34].

476 Spikes were detected as a minimum 10 mV elevation over the average depolarization during the pulse. For the
 477 mean action potential (AP) shape, varying spike forms from the initial (< 300 ms) part of the pulse were discarded.
 478 The extracted AP features were peak amplitude, threshold voltage and threshold time to peak (voltage derivative
 479 crossing 10 mV/ms), height (difference between peak and threshold), temporal width at half of the height and fast
 480 afterhyperpolarization (fAHP; a voltage dip of -0.5 mV or larger within 10 ms after the spike). For threshold and

481 fAHP detection, the spike shape was filtered with a digital 4th order Butterworth filter with critical frequencies 3.3 kHz,
482 respectively 1 kHz.

To understand, how much changes in capacitance affect the action potential generating currents, we compared the recorded spikes with hypothetical ones obtained by assuming unaltered currents with respect to the original near capacitance. For a target capacitance C_t , this hypothetical spike is a scaled version of the original spike,

$$V_{hypo}(t) = V_c(t_0) + \frac{C_c}{C_t} (V_c(t) - V_c(t_0)),$$

483 where $V_c(t)$ is the spike form at the original cell capacitance C_c and the initial time t_0 was chosen to be $t_{spike} - 3\text{ms}$
484 short before onset of the spike generating currents.

485 4.4 Simulations of the CapClamp

486 Simulations of neuron models coupled to the CapClamp were implemented using the neuron simulator Brian2 [81]
487 and the CapClamp was realized using the Brian2 provided NetworkOperation that updated the clamp current every
488 sampling interval using Equation 5 with zero delay between voltage sampling and current injection (for links to the
489 available code see Appendix).

490 4.4.1 Biophysical neuron model

491 In order to test the CapClamp in the presence of active ionic conductances, a Wang-Buzsáki (WB) neuron, a single
492 compartment model of hippocampal interneurons, was used [23]. Gating dynamics and peak conductances of the
493 transient sodium current and the delayed rectifier potassium current were modeled as described earlier [13, Appendix
494 A]. When the capacitance is varied, the WB neuron undergoes a well-characterized series of bifurcations; in particular it
495 exhibits a saddle-node loop (SNL) bifurcation at $C_m = 1.47 \frac{\mu\text{F}}{\text{cm}^2}$ [13, Fig. 6]. Here, the specific membrane capacitance
496 was chosen as $C_m = 0.75 \frac{\mu\text{F}}{\text{cm}^2} \frac{\mu\text{F}}{\text{cm}^2}$ and the membrane area was set to $A = 20000 \mu\text{m}^2$, so that the original cell
497 capacitance was 150 pF. Simulations were performed with the second order Runge-Kutta method, a time step of 1 μs
498 and dynamic clamp loop frequencies up to 100 kHz. Analysis of spike shapes was performed in the same way as for the
499 recorded cells.

500 4.4.2 Multicompartment model of a dentate gyrus granule cell

501 For a controlled test of the CapClamp in an electrotonically non-compact cell, a morphologically reconstruction of a
502 recorded DGGC was used as the basis for a multicompartment simulation. Soma and the two dendritic trees had a total
503 area of $14126 \mu\text{m}^2$. The axon was removed for the simulation. Membrane properties were assumed to be uniform and
504 chosen such that they reproduced the average values of the total capacitance and the membrane time constant observed
505 in the experiments: $C_m = \frac{C_n + C_f}{A} \approx 0.9 \frac{\mu\text{F}}{\text{cm}^2}$ and $R_m = \frac{\tau_0}{C_m} \approx 16800 \Omega\text{cm}^2$. The axial resistivity was chosen as
506 $R_a = 300 \Omega\text{cm}$. Simulations were performed with exponential Euler integration, a time step of 10 μs and a dynamic

507 clamp sampling frequency of 20 kHz. Capacitance measurement and clamp procedure were the same as in the recorded
508 DGGCs.

509 **5 Acknowledgements**

510 This work was supported by the German Ministry of Education and Research (grant no. 01GQ1403), the Deutsche
511 Forschungsgemeinschaft (DFG, German Research Foundation – Project numbers GRK 1589/2, EXC 257, FOR 2134)
512 and the European Research Council (grant no. 864243). We thank Jan Benda and Lukas Sonnenberg for their dedicated
513 support with dynamic clamp and fruitful discussions. We are grateful to Eve Marder and Ekaterina Morozova for
514 being able to test the RTX1 implementation of the CapClamp and apply the CapClamp in neurons of the crustacean
515 stomatogastric ganglion. We thank Robert Gowers and Philipp Norton for valuable feedback on the manuscript.

516 **6 Competing interests**

517 The authors declare that no competing interests exist.

518 7 Appendix

519 7.1 Impedance of a capacitance-clamped RC circuit

520 The impedance of a cell captures its response to the whole range of input frequencies (see Fig. 1 - suppl. 1). In
 521 the following, we derive the impedance of a passive membrane, an RC circuit, with capacitance C_c coupled to the
 522 CapClamp and compare it to the impedance of an RC circuit with the target capacitance C_t .

523 7.1.1 Analysis of the dynamic clamp via the Z-transform

In general, the dynamic clamp technique forms a digital filter, mapping the incoming sampled voltages to injected currents. For a sampling interval Δt , a linear mapping such as the CapClamp has the form

$$I_{dyn}(i\Delta t) = \sum_{j=0}^N \nu_j V((i-j)\Delta t) + \sum_{k=1}^M \gamma_k I_{dyn}((i-k)\Delta t), \quad (8)$$

524 where N and M determine history of voltage and current values, respectively, taken into account. For the CapClamp,
 525 the coefficients depend on cell capacitance C_c , target capacitance C_t and the sampling interval (see Eq. 5),

$$\begin{aligned} \nu_0 &= \frac{C_c - C_t}{C_t} \frac{C_c}{\Delta t}, \\ \nu_1 &= -\nu_0, \\ \gamma_1 &= -\frac{C_c - C_t}{C_t}. \end{aligned} \quad (9)$$

This linear mapping can be represented and analyzed using the Z-transform [82, Ch. 13],

$$\hat{I}(z) = F_{dyn}(z) \hat{V}(z), \quad (10)$$

where the transfer function follows from the properties of the Z-transform²

$$F_{dyn}(z) = \frac{\sum_{j=0}^N \nu_j z^{-j}}{1 - \sum_{k=1}^M \gamma_k z^{-k}}. \quad (11)$$

If the cell also forms a linear system, like the RC circuit, the transfer function of the coupled system (Fig. 6 A) is given by [82, Table 2.6]

$$H_{\text{cell+dyn}}(z) = \frac{H_{\text{cell}}(z)}{1 - H_{\text{cell}}(z)F_{\text{dyn}}(z)}, \quad (12)$$

526 where $H_{\text{cell}}(z)$ is the Z-transform of the membrane filter, e.g. $H_{\text{cell}}(z) = H_{\text{RC}}(z)$.

²A Z-transform $X_i \xrightarrow{Z} \hat{X}(z)$ is linear and has the delay property $X_{i-1} \xrightarrow{Z} z^{-1}\hat{X}(z)$ [82, Table 13.2].

The transfer function of the coupled system $H_{\text{cell+dyn}}(z)$ can then be compared with the one of the target system $H_{\text{target}}(z)$ (Fig. 6 B). Additionally, the frequency-dependent impedance can be retrieved from the transfer function by

$$Z_{\text{cell+dyn}}(f) = H_{\text{cell+dyn}}(e^{i2\pi f \Delta t}). \quad (13)$$

527 7.1.2 Transfer function of the CapClamp

The Z-transform of the CapClamp filter can be read directly from the general form of the transfer function (Eq. 11) and the CapClamp feedback coefficients (Eq. 9),

$$F_{\text{dyn}}(z) = \frac{C_c - C_t}{C_t} \frac{C_c}{\Delta t} \frac{1 - z^{-1}}{1 + \frac{C_c - C_t}{C_t} z^{-1}}. \quad (14)$$

528 7.1.3 Transfer function of the RC circuit

529 In an RC circuit, the dynamics of the voltage are

$$C \frac{dV}{dt} = -\frac{V}{R} + I.$$

530 Thus, in a single time step Δt , when the current is fixed, the voltage evolves as

$$V(k\Delta t) = V((k-1)\Delta t)e^{-\frac{\Delta t}{\tau}} + RI(1 - e^{-\frac{\Delta t}{\tau}}),$$

531 where $\tau = RC$ is the time constant. Applying the Z-transform results in the transfer function

$$H_{RC}(z) = R \left(1 - e^{-\frac{\Delta t}{\tau}}\right) \frac{1}{z - e^{-\frac{\Delta t}{\tau}}}, \quad (15)$$

532 which is subsequently used as the cell's transfer function $H_{\text{cell}}(z) = H_{RC}(z)$.

533 7.1.4 Transfer function of the clamped RC circuit

534 Introducing $K = \frac{C_c - C_t}{C_t}$ and $h_c = \frac{\Delta t}{\tau_c}$, the RC circuit (Eq. 15) and CapClamp (Eq. 14) transfer functions can be
535 combined using Equation 12 to get the transfer function of the combined system

$$H_{\text{cell+dyn}}(z) = R(1 - e^{-h_c}) \frac{z + K}{z^2 + (K - e^{-h_c} - \frac{1}{h_c} K(1 - e^{-h_c}))z - K(e^{-h_c} - \frac{1}{h_c}(1 - e^{-h_c}))}. \quad (16)$$

536 In comparison, the transfer function of the target RC circuit reads

$$H_{\text{target}}(z) = R(1 - e^{-h_t}) \frac{1}{z - e^{-h_t}}$$

537 with $h_t = \frac{\Delta t}{\tau_t} = \frac{\Delta t}{RC_t}$ reflecting the different target capacitance.

538 Figure 1 - suppl. 1 compares the resulting impedances for decreased and increased capacitances. As discussed in the
539 Results, the impedance amplitudes fit well up to a tenth of the dynamic clamp frequency. A closer look at the transfer
540 function explains the fit at low frequencies and the deviations at higher frequencies.

Input resistance is preserved The input resistance is equal to the impedance at zero frequency, that is at $z = e^{i2\pi 0} = 1$, which for both coupled and target system is the original resistance,

$$H_{\text{cell+dyn}}(1) = H_{\text{target}}(1) = R. \quad (17)$$

541 **Poles and zeros** For a further comparison, poles and zeros of the transfer functions are calculated. To simplify the
542 expressions, it is assumed that the time constant of the original and target circuits are much larger than the sampling
543 interval, that is $h_c \ll 1$ and $h_t \ll 1$.

Target circuit The target circuit has no zero and a single pole located at

$$p_t^{(1)} = e^{-h_t} = 1 - h_t + \dots \quad (18)$$

Capacitance clamped circuit The coupled system has one zero at

$$r_c^{(1)} = -K = 1 - \frac{C_c}{C_t}. \quad (19)$$

The clamped circuit has two poles at

$$p_c^{(1)} = 1 - (1 + K)h_c + \dots \quad (20)$$

and

$$p_c^{(2)} = \frac{K}{2}h_c + \dots \quad (21)$$

544 **Comparison of poles** All poles and zeros for an RC circuit in its original state and clamped at decreased and increased
545 capacitances are shown in Figure 6. The first pole of the clamped circuit coincides with the one of the target circuit:
546 $p_c^{(1)} = 1 - \frac{C_c}{C_t} \frac{\Delta t}{RC_c} = 1 - h_t = p_t^{(1)}$. As these pole lies close to $z = 1$, they determine the lower frequency response,
547 which explains why the impedance amplitudes fit so well in this range.

548 In addition to moving the existent pole of the cell circuit to the one of the target circuit, the CapClamp creates an
549 additional pole $p_c^{(2)} \approx \frac{h_c}{2} (\frac{C_c}{C_t} - 1)$ and a new zero $r_c^{(1)} = 1 - \frac{C_c}{C_t}$. Thus, at an increased capacitance $C_t > C_c$, the new
550 pole lies in the left half of the unit circle and thereby increases the impedance at higher frequencies. In contrast, at
551 a decreased capacitance, the additional zero moves into the left half of the complex plane and thereby decreases the
552 impedance at higher frequencies.

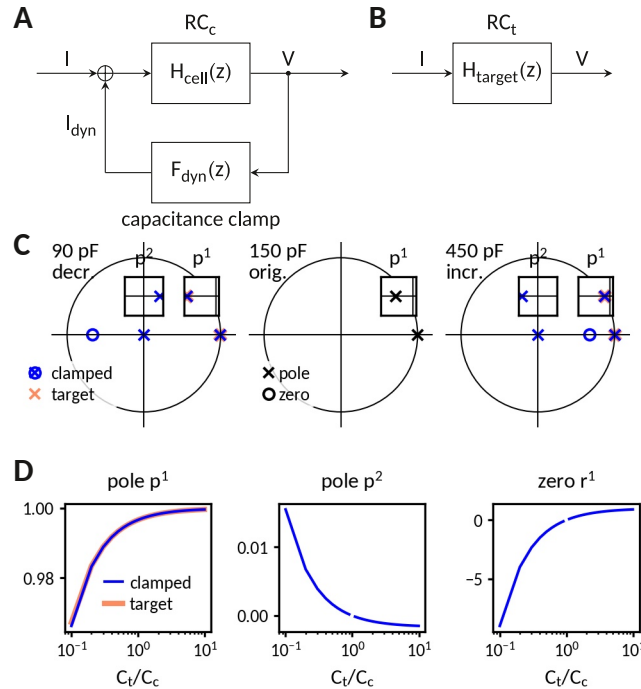


Figure 6: **Analysis of the capacitance clamp as a discrete feedback filter.** **A** Block diagram of the coupled system: RC circuit with original capacitance C_c and capacitance clamp feedback current. **B** Block diagram of the target system: RC circuit with target capacitance C_t . **C** Pole-zero plot of the transfer functions at a decreased (left), the original and an increased capacitance. In addition to mimicking the pole of the target system, the clamped system has an additional pole and an additional zero. **D** Pole and zero position versus capacitance.

553 **Stability** For the investigated RC circuit with $R=100\text{ M}\Omega$ and $C = 150\text{ pF}$ and a sampling interval of $50\text{ }\mu\text{s}$, both
 554 poles of the capacitance clamped system remain within the unit circle (Fig. 6) for the tested range from 0.1 to 10 times
 555 the original capacitance. As the coupled system is naturally causal, this implies that the transfer function of the clamped
 556 circuit is stable for this range of target capacitances, i.e. there are no unstable oscillations.

557 7.2 Mapping between a charging curve with two components and a two compartment circuit

558 In the following, we explain how a charging curve of a cell with two components can be mapped to the parameters of a
 559 two compartment circuit, which we used to extract the local capacitance in the recorded dentate gyrus granule cells
 560 (see Fig. 3). We first report the approach and results derived earlier [1, Appendix] and then explain how to extend the
 561 mapping when the capacitance is clamped to a modified value.

562 Golowasch et al. derived expressions for the near capacitance and the other circuit parameters by comparing the
 563 impedance of a two compartment circuit in Figure 3 A

$$Z(s) = \frac{1}{\frac{1}{R_n} + sC_n + \frac{1}{R_a + \frac{1}{\frac{1}{R_f} + sC_f}}} \quad (22)$$

564 with the impedance of a system whose response to a step currents is a sum of two exponentials

$$Z(s) = R_0 \frac{1}{1 + s\tau_0} + R_1 \frac{1}{1 + s\tau_1}. \quad (23)$$

565 The comparison of these two impedances gives four equations linking the circuit parameters and the two components of
566 the charging curve:

$$R_0 + R_1 = \frac{R_a R_n + R_f R_n}{R_a + R_f + R_n}, \quad (24)$$

$$R_0 \tau_0 + R_1 \tau_1 = \frac{R_a R_n R_f C_f}{R_a + R_f + R_n}, \quad (25)$$

$$\tau_0 + \tau_1 = \frac{(R_a + R_n) C_f R_f + (R_a + R_f) C_n R_n}{R_a + R_f + R_n}, \quad (26)$$

$$\tau_0 \tau_1 = \frac{R_a C_n R_n C_f R_f}{R_a + R_f + R_n}. \quad (27)$$

To solve this set of equations, they assume that the membrane time constant is the same in all compartments $C_n R_n = C_f R_f = \tau_c$. However in a clamped neuron, where the near capacitance is targeted to be modified to a k-fold different value, this equation becomes

$$C_n R_n = k C_f R_f, \quad (28)$$

567 where $k = \frac{C_{n,clam.}}{C_{n,orig.}}$.

568 For the unclamped case, $k = 1$, the mapping from the two components to the circuit parameters is

$$R_n = R_0 + \frac{\tau_0}{\tau_1} R_1, \quad (29)$$

$$C_n = \frac{\tau_0 \tau_1}{\tau_1 R_0 + \tau_0 R_1}, \quad (30)$$

$$R_f = \frac{R_0 \tau_1}{R_1 \tau_0} \left(R_0 + \frac{\tau_0}{\tau_1} R_1 \right) \quad (31)$$

$$C_f = \frac{R_1 \tau_0}{R_0 \tau_1} \frac{\tau_0 \tau_1}{\tau_1 R_0 + \tau_0 R_1} \quad (32)$$

$$R_a = \frac{\tau_1}{\tau_0 - \tau_1} \left(R_0 + \frac{\tau_0}{\tau_1} R_1 \right) \left(1 + \frac{R_0 \tau_1}{R_1 \tau_0} \right). \quad (33)$$

569 For the clamped case, $k \neq 1$, we used the python package sympy to solve the equations.

570 7.3 Adapted fitting procedure of dentate gyrus charging curves

571 The initial online capacitance measurement was based on fitting the charging curve at the beginning of the current pulse.

572 Posterior analysis showed an artefactual voltage drop of -0.2 mV starting about 0.2 ms before pulse onset (probably due

573 to coupling of the DAQ measurement card and the motherboard of the dynamic clamp computer), which limited the
 574 reliability of the online fit for cells with a small fast component. As no such artifact was observed for the recharging at
 575 the end of the pulse, this part was used in an improved offline fit. Additional measures to improve the fit were: cut of
 576 the first 0.2 ms after pulse end to minimize electrode artifacts, limiting the fit to the first 60 ms (3-4 times τ_0) after the
 577 pulse to prioritize the early part of the charging curve and a switch to the python package `lmfit` for better evaluation of
 578 parameter confidence bounds (`lmfit.github.io`). Furthermore, the finite rise time of the current injection by the amplifier
 579 was taken into account by adapting the original form of the charging curve (Eq. 6) to

$$V(t) = I_{ext} \left[\sum_{i; \tau_i \neq \tau_a} \frac{R_i}{\tau_i - \tau_a} \left(\tau_i \left(1 - e^{-\frac{t}{\tau_i}} \right) - \tau_a \left(1 - e^{-\frac{t}{\tau_a}} \right) \right) + \sum_{i; \tau_i = \tau_a} R_i \left(1 - e^{-\frac{t}{\tau_i}} - \frac{t}{\tau_i} e^{-\frac{t}{\tau_i}} \right) \right], \quad (34)$$

580 where the current rise time of the amplifier τ_a ($87 \pm 2 \mu\text{s}$) was obtained by fitting the recorded injected current for the
 581 current step command by a simple exponential. A comparison of the two exponential components and the resulting
 582 circuit parameters for the online and offline fitting procedures is shown in Tab. 3.

583 For the charging curves under capacitance clamp, the fitting procedure for the charging curve with two exponentials was
 584 initialized with values as expected for the targeted capacitance change: mapping the fitting results of the unclamped
 585 response to a two compartment circuit, changing the near capacitance to the targeted value and finally mapping this
 586 altered circuit back to the expected time scale and amplitudes. This initialization improved the fits especially at increased
 587 near capacitances, where the amplitude of the fast component becomes smaller.

Table 3: Comparison of online and offline fits to charging curves in the recorded dentate gyrus granule cells (N=18).

	online fit (mean \pm std)	offline fit (mean \pm std)
Two comp.		
τ_0	14.9 ± 4.8 ms	15.1 ± 4.8 ms
R_0	136.9 ± 47.5 M Ω	127.1 ± 44.6 M Ω
τ_1	0.41 ± 0.23 ms	0.77 ± 0.24 ms
R_1	25.1 ± 14.1 M Ω	34.5 ± 14.7 M Ω
Circuit		
C_n	14.9 ± 4.7 pF	21.0 ± 9.4 pF
R_n	1106.3 ± 519.3 M Ω	854.2 ± 394.0 M Ω
R_a	34.9 ± 19.9 M Ω	52.5 ± 19.8 M Ω
C_f	99.1 ± 33.7 pF	105.8 ± 33.0 pF

	online fit (mean \pm std)	offline fit (mean \pm std)
R_f	$159.6 \pm 58.1 \text{ M}\Omega$	$155.5 \pm 59.9 \text{ M}\Omega$

588 **7.4 Data and software availability**

- 589
- 590 • Electrophysiological recordings of capacitance clamped dentate gyrus granule cells: Paul Pfeiffer, & Federico
591 José Barreda Tomás. (2021). Capacitance clamp demonstration in rat dentate gyrus granule cells (1.0.0) [Data
592 set]. Zenodo. 10.5281/zenodo.5552207
 - 593 • Project repository with capacitance clamp module for RELACS and custom analysis/simulation in python:
594 Paul Pfeiffer, Federico José Barreda Tomás, Jiameng Wu, Jan-Hendrik Schleimer, Imre Vida, & Susanne
595 Schreiber. (2021). Software for: A dynamic clamp protocol to artificially modify cell capacitance (v1.0).
596 Zenodo. 10.5281/zenodo.5762092
 - 597 • Capacitance clamp plugin for RTXI, a real-time data-acquisition and control application for biological re-
598 search that allows to extend a conventional electrophysiology setup for dynamic clamp experiments [51]:
capacitance_clamp_rtxi_module: (v1.0.1). Zenodo. 10.5281/zenodo.5553946

599 **7.5 Supplementary figures**

- 600
- Figure 1 - suppl. 1: Impedance analysis of an RC circuit coupled to the capacitance clamp.

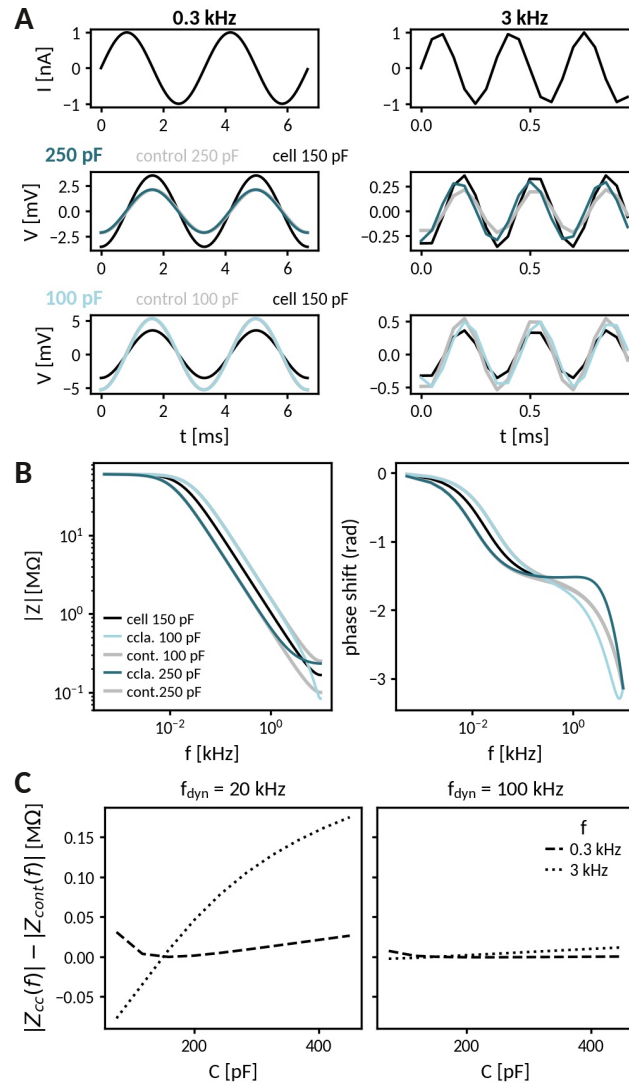


Figure 1 - suppl. 1: **Impedance analysis of an RC circuit coupled to the capacitance clamp.** **A** Injection of an oscillating current at 300 Hz (left) and at 3 kHz (right) to a passive cell (RC-circuit) with voltage responses clamped at an increased (middle) and a decreased capacitance (bottom). Black lines indicate the response of the cell at the original capacitance and gray lines those of the corresponding control cells. **B** Comparison of frequency-dependent impedance and phase shift of a cell at the above capacitances (black: cell capacitance, blues: clamped, gray: control). **C** Difference of impedances at 300 Hz (dotted) and 3 kHz (dashed) for clamped and control cell across different capacitances and for dynamic clamp frequencies of 20 kHz (left) and 100 kHz (right).

601 References

- 602 [1] J. Golowasch, G. Thomas, A. L. Taylor, A. Patel, A. Pineda, C. Khalil, and F. Nadim. Membrane Capacitance
603 Measurements Revisited: Dependence of Capacitance Value on Measurement Method in Nonisopotential Neurons.
604 *Journal of Neurophysiology*, 102(4):2161–2175, 2009. ISSN 0022-3077. doi:10.1152/jn.00160.2009.
- 605 [2] W. E. White and S. L. Hooper. Contamination of current-clamp measurement of neuron capacitance by
606 voltage-dependent phenomena. *Journal of Neurophysiology*, 110(1):257–268, 2013. ISSN 0022-3077.
607 doi:10.1152/jn.00993.2012.
- 608 [3] Luc J. Gentet, Greg J. Stuart, and John D. Clements. Direct Measurement of Specific Membrane Capacitance in
609 Neurons. *Biophysical Journal*, 79(1):314–320, July 2000. ISSN 00063495. doi:10.1016/S0006-3495(00)76293-X.
- 610 [4] D.K. Hartline and D.R. Colman. Rapid Conduction and the Evolution of Giant Axons and Myelinated Fibers.
611 *Current Biology*, 17(1):R29–R35, January 2007. ISSN 09609822. doi:10.1016/j.cub.2006.11.042.
- 612 [5] R. Douglas Fields. White matter in learning, cognition and psychiatric disorders. *Trends in Neurosciences*, 31(7):
613 361–370, July 2008. ISSN 01662236. doi:10.1016/j.tins.2008.04.001.
- 614 [6] Guy Eyal, Matthijs B. Verhoog, Guilherme Testa-Silva, Yair Deitcher, Johannes C. Lodder, Ruth Benavides-
615 Piccione, Juan Morales, Javier Defelipe, Christiaan P.J. de Kock, Huibert D. Mansvelder, and Idan Segev. Unique
616 membrane properties and enhanced signal processing in human neocortical neurons. *eLife*, 5:1–18, 2016. ISSN
617 2050084X. doi:10.7554/eLife.16553.
- 618 [7] Lou Beaulieu-Laroche, Enrique H.S. Toloza, Marie-Sophie van der Goes, Mathieu Lafourcade, Derrick Barnagian,
619 Ziv M. Williams, Emad N. Eskandar, Matthew P. Frosch, Sydney S. Cash, and Mark T. Harnett. Enhanced
620 Dendritic Compartmentalization in Human Cortical Neurons. *Cell*, 175(3):643–651.e14, October 2018. ISSN
621 00928674. doi:10.1016/j.cell.2018.08.045.
- 622 [8] Hugh P.C. Robinson. Conductance injection. *Trends in Neurosciences*, 17(4):147, January 1994. ISSN 01662236.
623 doi:10.1016/0166-2236(94)90088-4.
- 624 [9] Andrew A. Sharp, Michael B. O’Neil, L. F. Abbott, and Eve Marder. The dynamic clamp: Artificial conductances
625 in biological neurons. *Trends in Neurosciences*, 16(10):389–394, 1993. ISSN 01662236. doi:10.1016/0166-
626 2236(93)90004-6.
- 627 [10] David B. Jaffe and Robert Brenner. A computational model for how the fast afterhyperpolarization paradoxically
628 increases gain in regularly firing neurons. *Journal of Neurophysiology*, 119(4):1506–1520, April 2018. ISSN
629 0022-3077, 1522-1598. doi:10.1152/jn.00385.2017.
- 630 [11] Alessio Franci, Guillaume Drion, and Rodolphe Sepulchre. Robust and tunable bursting requires slow pos-
631 itive feedback. *Journal of Neurophysiology*, 119(3):1222–1234, March 2018. ISSN 0022-3077, 1522-1598.
632 doi:10.1152/jn.00804.2017.

-
- 633 [12] Christoph Kirst, Julian Ammer, Felix Felmy, Andreas Herz, and Martin Stemmler. Fundamental Structure and
634 Modulation of Neuronal Excitability: Synaptic Control of Coding, Resonance, and Network Synchronization.
635 *BioRxiv*, July 2015. doi:10.1101/022475.
- 636 [13] Janina Hesse, Jan Hendrik Schleimer, and Susanne Schreiber. Qualitative changes in phase-response curve
637 and synchronization at the saddle-node-loop bifurcation. *Physical Review E*, 95(5), 2017. ISSN 24700053.
638 doi:10.1103/PhysRevE.95.052203.
- 639 [14] Susana Andrea Contreras, Jan-Hendrik Schleimer, Allan T. Gullledge, and Susanne Schreiber. Activity-mediated
640 accumulation of potassium induces a switch in firing pattern and neuronal excitability type. *BioRxiv*, November
641 2020. doi:10.1101/2020.11.30.403782.
- 642 [15] Astrid A. Prinz, L. F. Abbott, and Eve Marder. The dynamic clamp comes of age. *Trends in Neurosciences*, 27(4):
643 218–224, 2004. ISSN 01662236. doi:10.1016/j.tins.2004.02.004.
- 644 [16] M. N. Economo, F. R. Fernandez, and J. A. White. Dynamic Clamp: Alteration of Response Properties and
645 Creation of Virtual Realities in Neurophysiology. *Journal of Neuroscience*, 30(7):2407–2413, 2010. ISSN
646 0270-6474. doi:10.1523/jneurosci.5954-09.2010.
- 647 [17] Gina G Turrigiano, Eve Marder, and L F Abbott. Cellular short-term memory from a slow potassium conductance.
648 *Journal of Neurophysiology*, 75(2):963–6, 1996. ISSN 0022-3077. doi:10.1152/jn.1996.75.2.963.
- 649 [18] Gytis Svirskis, Vibhakar Kotak, Dan H Sanes, and John Rinzel. Sodium Along With Low-Threshold Potas-
650 sium Currents Enhance Coincidence Detection of Subthreshold Noisy Signals in MSO Neurons. *Journal of*
651 *Neurophysiology*, 91:9, 2004. doi:10.1152/jn.00717.2003.
- 652 [19] Steven A. Prescott, Stéphanie Ratté, Yves De Koninck, and Terrence J. Sejnowski. Pyramidal Neurons Switch
653 From Integrators In Vitro to Resonators Under In Vivo-Like Conditions. *Journal of Neurophysiology*, 100(6):
654 3030–3042, December 2008. ISSN 0022-3077, 1522-1598. doi:10.1152/jn.90634.2008.
- 655 [20] A. Hasenstaub, S. Otte, E. Callaway, and T. J. Sejnowski. Metabolic cost as a unifying principle governing
656 neuronal biophysics. *Proceedings of the National Academy of Sciences*, 107(27):12329–12334, July 2010. ISSN
657 0027-8424, 1091-6490. doi:10.1073/pnas.0914886107.
- 658 [21] Attila Szűcs, Anikó Rátkai, Katalin Schlett, and Ramon Huerta. Frequency-dependent regulation of intrinsic
659 excitability by voltage-activated membrane conductances, computational modeling and dynamic clamp. *European*
660 *Journal of Neuroscience*, 46(9):2429–2444, 2017. ISSN 14609568. doi:10.1111/ejn.13708.
- 661 [22] Paul Pfeiffer, Alexei V Egorov, Franziska Lorenz, Jan-Hendrik Schleimer, Andreas Draguhn, and Susanne
662 Schreiber. Clusters of cooperative ion channels enable a membrane-potential-based mechanism for short-term
663 memory. *eLife*, 9:e49974, February 2020. ISSN 2050-084X. doi:10.7554/eLife.49974.
- 664 [23] Xiao-Jing Wang and György Buzsáki. Gamma Oscillation by Synaptic Inhibition in a Hippocampal Interneuronal
665 Network Model. *Journal of Neuroscience*, 16(20):6402–6413, October 1996. ISSN 0270-6474, 1529-2401.
666 doi:10.1523/JNEUROSCI.16-20-06402.1996.

-
- 667 [24] Laura L. Rihn and Brenda J. Claiborne. Dendritic growth and regression in rat dentate granule cells during
668 late postnatal development. *Developmental Brain Research*, 54(1):115–124, June 1990. ISSN 01653806.
669 doi:10.1016/0165-3806(90)90071-6.
- 670 [25] C. Schmidt-Hieber, P. Jonas, and J. Bischofberger. Subthreshold Dendritic Signal Processing and Coincidence
671 Detection in Dentate Gyrus Granule Cells. *Journal of Neuroscience*, 27(31):8430–8441, August 2007. ISSN
672 0270-6474, 1529-2401. doi:10.1523/JNEUROSCI.1787-07.2007.
- 673 [26] Willem A. M. Wybo, Benjamin Torben-Nielsen, Thomas Nevian, and Marc-Oliver Gewaltig. Electrical
674 Compartmentalization in Neurons. *Cell Reports*, 26(7):1759–1773.e7, February 2019. ISSN 2211-1247.
675 doi:10.1016/j.celrep.2019.01.074.
- 676 [27] Roland Krueppel, Stefan Remy, and Heinz Beck. Dendritic Integration in Hippocampal Dentate Granule Cells.
677 *Neuron*, 71(3):512–528, August 2011. ISSN 08966273. doi:10.1016/j.neuron.2011.05.043.
- 678 [28] Jegath C Athilingam, Roy Ben-Shalom, Caroline M Keeshen, Vikaas S Sohal, and Kevin J Bender. Serotonin
679 enhances excitability and gamma frequency temporal integration in mouse prefrontal fast-spiking interneurons.
680 *eLife*, 6:e31991, December 2017. ISSN 2050-084X. doi:10.7554/eLife.31991.
- 681 [29] Go Ashida, Kousuke Abe, Kazuo Funabiki, and Masakazu Konishi. Passive Soma Facilitates Submillisecond
682 Coincidence Detection in the Owl’s Auditory System. *Journal of Neurophysiology*, 97(3):2267–2282, March
683 2007. ISSN 0022-3077, 1522-1598. doi:10.1152/jn.00399.2006.
- 684 [30] Simon B. Laughlin, Rob R. de Ruyter van Steveninck, and John C. Anderson. The metabolic cost of neural
685 information. *Nature Neuroscience*, 1(1):36–41, May 1998. ISSN 1097-6256, 1546-1726. doi:10.1038/236.
- 686 [31] Bhanu P. Tewari, Lata Chaunsali, Susan L. Campbell, Dipan C. Patel, Adam E. Goode, and Harald Sontheimer.
687 Perineuronal nets decrease membrane capacitance of peritumoral fast spiking interneurons in a model of epilepsy.
688 *Nature Communications*, 9(1):4724, December 2018. ISSN 2041-1723. doi:10.1038/s41467-018-07113-0.
- 689 [32] Klaus M. Stiefel, Boris S. Gutkin, and Terrence J. Sejnowski. Cholinergic Neuromodulation Changes Phase
690 Response Curve Shape and Type in Cortical Pyramidal Neurons. *PLOS ONE*, 3(12):e3947, December 2008. ISSN
691 1932-6203. doi:10.1371/journal.pone.0003947.
- 692 [33] Klaus M. Stiefel, Boris S. Gutkin, and Terrence J. Sejnowski. The effects of cholinergic neuromodulation on
693 neuronal phase-response curves of modeled cortical neurons. *Journal of Computational Neuroscience*, 26(2):
694 289–301, April 2009. ISSN 0929-5313, 1573-6873. doi:10.1007/s10827-008-0111-9.
- 695 [34] Eugene M. Izhikevich. *Dynamical Systems in Neuroscience: The Geometry of Excitability and Bursting*. The MIT
696 Press, 2006. ISBN 978-0-262-27607-8. doi:10.7551/mitpress/2526.001.0001.
- 697 [35] Steven A. Prescott, Yves De Koninck, and Terrence J. Sejnowski. Biophysical Basis for Three Distinct Dynamical
698 Mechanisms of Action Potential Initiation. *PLOS Computational Biology*, 4(10):e1000198, October 2008. ISSN
699 1553-7358. doi:10.1371/journal.pcbi.1000198.

- 700 [36] Ronald Wilders. Dynamic clamp: A powerful tool in cardiac electrophysiology. *The Journal of Physiology*, 576
701 (2):349–359, October 2006. ISSN 00223751. doi:10.1113/jphysiol.2006.115840.
- 702 [37] J. M. Bekkers and M. Hausser. Targeted dendrotomy reveals active and passive contributions of the dendritic
703 tree to synaptic integration and neuronal output. *Proceedings of the National Academy of Sciences*, 104(27):
704 11447–11452, July 2007. ISSN 0027-8424, 1091-6490. doi:10.1073/pnas.0701586104.
- 705 [38] Miklos Szoboszlay, Andrea Lőrincz, Frederic Lanore, Koen Vervaeke, R. Angus Silver, and Zoltan Nusser.
706 Functional Properties of Dendritic Gap Junctions in Cerebellar Golgi Cells. *Neuron*, 90(5):1043–1056, June 2016.
707 ISSN 08966273. doi:10.1016/j.neuron.2016.03.029.
- 708 [39] Jia Liu, Yoon Seok Kim, Claire E. Richardson, Ariane Tom, Charu Ramakrishnan, Fikri Birey, Toru Katsumata,
709 Shucheng Chen, Cheng Wang, Xiao Wang, Lydia-Marie Joubert, Yuenwen Jiang, Huiliang Wang, Lief E. Fenno,
710 Jeffrey B.-H. Tok, Sergiu P. Pașca, Kang Shen, Zhenan Bao, and Karl Deisseroth. Genetically targeted chemical
711 assembly of functional materials in living cells, tissues, and animals. *Science*, 367(6484):1372, March 2020.
712 doi:10.1126/science.aay4866.
- 713 [40] Bernardo L. de Oliveira, Emily R. Pfeiffer, Joakim Sundnes, Samuel T. Wall, and Andrew D. McCulloch. Increased
714 Cell Membrane Capacitance is the Dominant Mechanism of Stretch-Dependent Conduction Slowing in the Rabbit
715 Heart: A Computational Study. *Cellular and Molecular Bioengineering*, 8(2):237–246, June 2015. ISSN
716 1865-5025, 1865-5033. doi:10.1007/s12195-015-0384-9.
- 717 [41] Hillel Ori, Hananel Hazan, Eve Marder, and Shimon Marom. Dynamic clamp constructed phase diagram for the
718 Hodgkin and Huxley model of excitability. *Proceedings of the National Academy of Sciences*, 117(7):3575–3582,
719 February 2020. ISSN 0027-8424, 1091-6490. doi:10.1073/pnas.1916514117.
- 720 [42] Janina Hesse and Susanne Schreiber. Externalization of neuronal somata as an evolutionary strategy for energy
721 economization. *Current Biology*, 25(8):R324–R325, 2015. ISSN 09609822. doi:10.1016/j.cub.2015.02.024.
- 722 [43] D H Edwards and B Mulloney. Compartmental models of electrotonic structure and synaptic integra-
723 tion in an identified neurone. *The Journal of Physiology*, 348(1):89–113, March 1984. ISSN 00223751.
724 doi:10.1113/jphysiol.1984.sp015101.
- 725 [44] Willem AM Wybo, Jakob Jordan, Benjamin Ellenberger, Ulisses Marti Mengual, Thomas Nevian, and Walter
726 Senn. Data-driven reduction of dendritic morphologies with preserved dendro-somatic responses. *eLife*, 10:
727 e60936, January 2021. ISSN 2050-084X. doi:10.7554/eLife.60936.
- 728 [45] A. Norenberg, H. Hu, I. Vida, M. Bartos, and P. Jonas. Distinct nonuniform cable properties optimize rapid and
729 efficient activation of fast-spiking GABAergic interneurons. *Proceedings of the National Academy of Sciences*,
730 107(2):894–899, January 2010. ISSN 0027-8424, 1091-6490. doi:10.1073/pnas.0910716107.
- 731 [46] Laurent Badel, Sandrine Lefort, Romain Brette, Carl C H Petersen, Wulfram Gerstner, and Magnus J E Richardson.
732 Dynamic I-V Curves Are Reliable Predictors of Naturalistic Pyramidal-Neuron Voltage Traces. *J Neurophysiol*,
733 99:11, 2008.

-
- 734 [47] Alan D Dorval, David J Christini, and John A White. Real-Time Linux Dynamic Clamp: A Fast and Flexible Way
735 to Construct Virtual Ion Channels in Living Cells. *Annals of Biomedical Engineering*, 29:11, 2001.
- 736 [48] Jan Benda, Tim Gollisch, Christian K Machens, and Andreas VM Herz. From response to stimulus: Adaptive
737 sampling in sensory physiology. *Current Opinion in Neurobiology*, 17(4):430–436, August 2007. ISSN 09594388.
738 doi:10.1016/j.conb.2007.07.009.
- 739 [49] Ildikó Kemenes, Vincenzo Marra, Michael Crossley, Dávid Samu, Kevin Staras, György Kemenes, and Thomas
740 Nowotny. Dynamic clamp with StdpC software. *Nature Protocols*, 6(3):405–417, March 2011. ISSN 1750-2799.
741 doi:10.1038/nprot.2010.200.
- 742 [50] Daniele Linaro, João Couto, and Michele Giugliano. Real-time Electrophysiology: Using Closed-loop Protocols
743 to Probe Neuronal Dynamics and Beyond. *Journal of Visualized Experiments*, (100):52320, June 2015. ISSN
744 1940-087X. doi:10.3791/52320.
- 745 [51] Yogi A. Patel, Ansel George, Alan D. Dorval, John A. White, David J. Christini, and Robert J. Butera. Hard
746 real-time closed-loop electrophysiology with the Real-Time eXperiment Interface (RTXI). *PLOS Computational*
747 *Biology*, 13(5):e1005430, 2017. ISSN 1553-7358. doi:10.1371/journal.pcbi.1005430.
- 748 [52] Niraj S. Desai, Richard Gray, and Daniel Johnston. A Dynamic Clamp on Every Rig. *eneuro*, 4(5):ENEURO.0250–
749 17.2017, September 2017. ISSN 2373-2822. doi:10.1523/ENEURO.0250-17.2017.
- 750 [53] Rodrigo Amaducci, Manuel Reyes-Sanchez, Irene Elices, Francisco B. Rodriguez, and Pablo Varona. RTHybrid:
751 A Standardized and Open-Source Real-Time Software Model Library for Experimental Neuroscience. *Frontiers*
752 *in Neuroinformatics*, 13:11, March 2019. ISSN 1662-5196. doi:10.3389/fninf.2019.00011.
- 753 [54] Jonathan C. Bettencourt, Kyle P. Lillis, Laura R. Stupin, and John A. White. Effects of imperfect dynamic
754 clamp: Computational and experimental results. *Journal of Neuroscience Methods*, 169(2):282–289, 2008. ISSN
755 08966273. doi:10.1016/j.jneumeth.2007.10.009.
- 756 [55] Romain Brette, Zuzanna Piwkowska, Cyril Monier, Michelle Rudolph-Lilith, Julien Fournier, Manuel Levy,
757 Yves Frégnac, Thierry Bal, and Alain Destexhe. High-Resolution Intracellular Recordings Using a Real-
758 Time Computational Model of the Electrode. *Neuron*, 59(3):379–391, August 2008. ISSN 08966273.
759 doi:10.1016/j.neuron.2008.06.021.
- 760 [56] Thierry Bal and Alain Destexhe, editors. *Dynamic-Clamp: From Principles to Applications*. Springer US, New
761 York, NY, 2009. ISBN 978-0-387-89278-8 978-0-387-89279-5. doi:10.1007/978-0-387-89279-5.
- 762 [57] Florin Amzica and Dag Neckelmann. Membrane Capacitance of Cortical Neurons and Glia During Sleep
763 Oscillations and Spike-Wave Seizures. *Journal of Neurophysiology*, 82(5):2731–2746, 1999. ISSN 0022-3077.
764 doi:10.1152/jn.1999.82.5.2731.
- 765 [58] Biswa Sengupta, Martin Stemmler, Simon B. Laughlin, and Jeremy E. Niven. Action Potential Energy Efficiency
766 Varies Among Neuron Types in Vertebrates and Invertebrates. *PLOS Computational Biology*, 6(7):e1000840, July
767 2010. ISSN 1553-7358. doi:10.1371/journal.pcbi.1000840.

-
- 768 [59] Ann M. Castelfranco and Daniel K. Hartline. The evolution of vertebrate and invertebrate myelin: A theoretical
769 computational study. *Journal of Computational Neuroscience*, 38(3):521–538, June 2015. ISSN 0929-5313,
770 1573-6873. doi:10.1007/s10827-015-0552-x.
- 771 [60] William F Podlaski, Alexander Seeholzer, Lukas N Groschner, Gero Miesenböck, Rajnish Ranjan, and Tim P
772 Vogels. Mapping the function of neuronal ion channels in model and experiment. *eLife*, 6:e22152, March 2017.
773 ISSN 2050-084X. doi:10.7554/eLife.22152.
- 774 [61] Nathan W. Gouwens, Jim Berg, David Feng, Staci A. Sorensen, Hongkui Zeng, Michael J. Hawrylycz, Christof
775 Koch, and Anton Arkhipov. Systematic generation of biophysically detailed models for diverse cortical neuron
776 types. *Nature Communications*, 9(1):710, December 2018. ISSN 2041-1723. doi:10.1038/s41467-017-02718-3.
- 777 [62] Mikhail G. Shapiro, Kazuaki Homma, Sebastian Villarreal, Claus Peter Richter, and Francisco Bezanilla. Infrared
778 light excites cells by changing their electrical capacitance. *Nature communications*, 8:16148, 2017. ISSN
779 20411723. doi:10.1038/ncomms16148.
- 780 [63] João L. Carvalho-de-Souza, Bernardo I. Pinto, David R. Pepperberg, and Francisco Bezanilla. Optocapacitive
781 Generation of Action Potentials by Microsecond Laser Pulses of Nanojoule Energy. *Biophysical Journal*, 114(2):
782 283–288, 2018. ISSN 15420086. doi:10.1016/j.bpj.2017.11.018.
- 783 [64] B. Krasovitski, V. Frenkel, S. Shoham, and E. Kimmel. Intramembrane cavitation as a unifying mechanism for
784 ultrasound-induced bioeffects. *Proceedings of the National Academy of Sciences*, 108(8):3258–3263, February
785 2011. ISSN 0027-8424, 1091-6490. doi:10.1073/pnas.1015771108.
- 786 [65] Michael Plaksin, Shy Shoham, and Eitan Kimmel. Intramembrane Cavitation as a Predictive Bio-Piezoelectric
787 Mechanism for Ultrasonic Brain Stimulation. *Physical Review X*, 4(1):011004, January 2014. ISSN 2160-3308.
788 doi:10.1103/PhysRevX.4.011004.
- 789 [66] Timothy O’Leary, Alex H. Williams, Alessio Franci, and Eve Marder. Cell Types, Network Homeostasis, and
790 Pathological Compensation from a Biologically Plausible Ion Channel Expression Model. *Neuron*, 82(4):809–821,
791 2014. ISSN 10974199. doi:10.1016/j.neuron.2014.04.002.
- 792 [67] Simone Temporal, Kawasi M. Lett, and David J. Schulz. Activity-Dependent Feedback Regulates Correlated Ion
793 Channel mRNA Levels in Single Identified Motor Neurons. *Current Biology*, 24(16):1899–1904, August 2014.
794 ISSN 09609822. doi:10.1016/j.cub.2014.06.067.
- 795 [68] Joseph M. Santin and David J. Schulz. Membrane Voltage Is a Direct Feedback Signal That Influences Correlated
796 Ion Channel Expression in Neurons. *Current Biology*, 29(10):1683–1688.e2, May 2019. ISSN 09609822.
797 doi:10.1016/j.cub.2019.04.008.
- 798 [69] Pablo Chamorro, Carlos Muñiz, Rafael Levi, David Arroyo, Francisco B. Rodríguez, and Pablo Varona. General-
799 ization of the Dynamic Clamp Concept in Neurophysiology and Behavior. *PLOS ONE*, 7(7):e40887, July 2012.
800 ISSN 1932-6203. doi:10.1371/journal.pone.0040887.

-
- 801 [70] Ghanim Ullah and Steven J. Schiff. Tracking and control of neuronal Hodgkin-Huxley dynamics. *Physical Review E - Statistical, Nonlinear, and Soft Matter Physics*, 79(4):1–4, 2009. ISSN 15393755.
802
803 doi:10.1103/PhysRevE.79.040901.
- 804 [71] Catalina Rivera, Hyuck-Jin Kwon, Ali Hashmi, Gan Yu, Jiheng Zhao, Jianlong Gao, Jie Xu, Wei Xue, and
805 Alexander Dimitrov. Towards a Dynamic Clamp for Neurochemical Modalities. *Sensors*, 15(5):10465–10480,
806 May 2015. ISSN 1424-8220. doi:10.3390/s150510465.
- 807 [72] Patrick Harrigan, Hiten D. Madhani, and Hana El-Samad. Real-Time Genetic Compensation Defines the
808 Dynamic Demands of Feedback Control. *Cell*, 175(3):877–886.e10, October 2018. ISSN 00928674.
809 doi:10.1016/j.cell.2018.09.044.
- 810 [73] Jonathan P Newman, Ming-fai Fong, Daniel C Millard, Clarissa J Whitmire, Garrett B Stanley, and Steve M
811 Potter. Optogenetic feedback control of neural activity. *eLife*, 4:e07192, July 2015. ISSN 2050-084X.
812 doi:10.7554/eLife.07192.
- 813 [74] David Hocker and Il Memming Park. Myopic control of neural dynamics. *PLOS Computational Biology*, 15(3):
814 e1006854, March 2019. ISSN 1553-7358. doi:10.1371/journal.pcbi.1006854.
- 815 [75] Dan Bar-Yehuda and Alon Korngreen. Space-Clamp Problems When Voltage Clamping Neurons Expressing
816 Voltage-Gated Conductances. *Journal of Neurophysiology*, 99(3):1127–1136, March 2008. ISSN 0022-3077,
817 1522-1598. doi:10.1152/jn.01232.2007.
- 818 [76] Guy Major, Jonathan D Evans, and J Julian B Jack. Solutions for Transients in Arbitrarily Branching Cables: 1.
819 Voltage Recording with a Somatic Shunt. *Biophysical Journal*, 65:27, 1993. doi:10.1016/S0006-3495(93)81037-3.
- 820 [77] Sam A. Booker, Jie Song, and Imre Vida. Whole-cell Patch-clamp Recordings from Morphologically- and
821 Neurochemically-identified Hippocampal Interneurons. *Journal of Visualized Experiments*, (91):51706, September
822 2014. ISSN 1940-087X. doi:10.3791/51706.
- 823 [78] Linqing Feng, Ting Zhao, and Jinhyun Kim. neuTube 1.0: A New Design for Efficient Neuron Reconstruction
824 Software Based on the SWC Format. *eneuro*, 2(1):ENEURO.0049–14.2014, January 2015. ISSN 2373-2822.
825 doi:10.1523/ENEURO.0049-14.2014.
- 826 [79] SciPy 1.0 Contributors, Pauli Virtanen, Ralf Gommers, Travis E. Oliphant, Matt Haberland, Tyler Reddy, David
827 Cournapeau, Evgeni Burovski, Pearu Peterson, Warren Weckesser, Jonathan Bright, Stéfan J. van der Walt,
828 Matthew Brett, Joshua Wilson, K. Jarrod Millman, Nikolay Mayorov, Andrew R. J. Nelson, Eric Jones, Robert
829 Kern, Eric Larson, C J Carey, İlhan Polat, Yu Feng, Eric W. Moore, Jake VanderPlas, Denis Laxalde, Josef Perktold,
830 Robert Cimrman, Ian Henriksen, E. A. Quintero, Charles R. Harris, Anne M. Archibald, Antônio H. Ribeiro,
831 Fabian Pedregosa, and Paul van Mulbregt. SciPy 1.0: Fundamental algorithms for scientific computing in Python.
832 *Nature Methods*, 17(3):261–272, March 2020. ISSN 1548-7091, 1548-7105. doi:10.1038/s41592-019-0686-2.
- 833 [80] W G Bardsley, P B McGinlay, and A J Wright. The F test for model discrimination with exponential functions.
834 *Biometrika*, 73(2):8, 1986. doi:10.2307/2336228.

- 835 [81] Marcel Stimberg, Romain Brette, and Dan FM Goodman. Brian 2, an intuitive and efficient neural simulator.
836 *eLife*, 8:e47314, August 2019. ISSN 2050-084X. doi:10.7554/eLife.47314.
- 837 [82] Richard Dorf and Robert Bishop. *Modern Control Systems*. Pearson, twelfth edition, 2010. ISBN 978-0-13-
838 602458-3.